Distribution Agreement

Signature: ______________________________

Pushkar Shinde March 26, 2022

Developing and Understanding Nucleic Acid Tension Sensors to Dissect Cellular Mechanosensing

By

Pushkar Shinde

Chemistry

Khalid Salaita, Ph.D.
Advisor

Matthew Weinschenk, Ph.D.
Committee Member

James Kindt, Ph.D.
Committee Member

2022

Developing and Understanding Nucleic Acid Tension Sensors to Dissect Cellular Mechanosensing

By

Pushkar Shinde

Khalid Salaita, Ph.D.
Advisor

An abstract of
A thesis submitted to the Faculty of the Emory College of Arts and Sciences in partial fulfillment of the requirements for the degree of Bachelor of Sciences with Honors

Chemistry

2022

Abstract

Developing and Understanding Nucleic Acid Tension Sensors to Dissect Cellular Mechanosensing

By Pushkar Shinde

Five chapters comprise this thesis. The first provides a motivation for studying mechanobiology and introduces the tools and techniques: Molecular Tension Fluorescence Microscopy and nucleic acid tension probes. The second chapter explores the relationship between nucleic acid tension probe structure and function through molecular dynamics simulations. These data suggest that subtle sequence variations lead to significant structural alterations that can tune probe photophysical properties without significantly affecting mechanics. The third chapter designs and explores a mathematical model of a set of nucleic acid tension probes to measure bond lifetime. The results suggest these probes may be feasible and outlines several challenges that would need to be overcome to facilitate their implementation. The fourth chapter develops probes with the same force to open but dramatically different work thresholds, to understand the fundamental mechanisms of T-cell triggering. The results suggest that the T-Cell Receptor (TCR) responds to more than force, though further experimentation is required to understand exactly what the TCR senses. The final chapter briefly summarizes the work and places it in a larger context. Holistically, this work aims to help advance mechanobiology by exploring the relationships between tension probe structure, the physical parameters to which these probes respond, the mechanical stimulus these probes present receptors, and receptors’ responses to those stimuli.

Developing and Understanding Nucleic Acid Tension Sensors to Dissect Cellular Mechanosensing

By

Pushkar Shinde

Khalid Salaita, Ph.D.
Advisor

A thesis submitted to the Faculty of the Emory College of Arts and Sciences in partial fulfillment of the requirements for the degree of Bachelor of Sciences with Honors

Chemistry

2022

Acknowledgements

This journey would have been impossible without the support of a constellation of people far too numerous to enumerate in this short space. I would like to begin by acknowledging my PI, Dr. Khalid Salaita, who graciously allowed me to join his laboratory and, through his mentorship, encouraged my curiosity, sharpened my understanding, and broadened my field of view.

I would also like to thank my committee members Dr. Matthew Weinschenk and Dr. James Kindt. I am deeply grateful for their willingness to engage my questions and make time for my learning, whether in this project, in classes, or beyond.

The Salaita Lab community has also been essential to this path – the group's collaborative spirit and insights have profoundly influenced my scientific approach. Dale Combs' mentorship through most of the T-cell project was transformative; his combination of patience in answering questions and generosity with his time in lab empowered me to begin to grapple with complex questions surrounding T-cell activation. Dr. Roxanne Glazier's extraordinary mentorship, time, and advice, both during the tension probe structure project and beyond inspire me to become a more meticulous scientist. Dr. Aaron Blanchard helped teach me to dissect systems mathematically. Anna Kellner introduced me to the field of mechanobiology, sharpened my ideas, and taught me to understand and execute its experimental techniques. Dr. Joshua Brockman, Dr. Rong Ma, Rachel Bender, Dr. Hiroaki Ogasewara, and Arventh Velusamy often provided invaluable advice – whether technical, analytical, or existential. In addition, through involving me in Cover Art Submissions, Roxanne, Josh, Rachel, Selma Piranej and Dr. Hanquan Su kindly provided me the opportunity to learn to communicate science more effectively through images.

Finally, I would like to thank my parents: you've made me.

Table of Contents

Table of Figures

Chapter 1: Introduction

Chapter 2: Understanding Tension Probe Structure and Function

Chapter 3: Mathematically Modelling Probes to Measure Bond Lifetime

Chapter 4: Tension Probes to Disentangle Force and Work in T-Cell Receptor Triggering

Chapter 1: Introduction

Life moves.

Living systems exists in a physical world – they constantly sense and respond to their mechanical environment in precise ways. Cells are no exception: stem cells differentiate differently depending on the stiffness of the underlying substrate [3]; fibroblasts alter expression of ECM proteins in response to mechanical stresses [4]; T-cells actively move through tissue [5], using forces to identify and eliminate pathogens [6, 7]. At an even smaller level, mechanics are fundamental to protein function. Helicases generate force as they act on DNA [8]; von Willebrand's Factor elongates under shear flow to help trigger platelet recruitment [9]; integrins can change conformations under force to alter binding affinities and signaling [3, 10]. Mechanics aren't a haphazard addition, but rather represent an essential component of many of life's most fundamental interactions.

While the idea that mechanics influence biology traces back over a century to D'Arcy Thompson, relatively recent technological advances empowered researchers to study cells' deployment and response to mechanical stimuli with increasing resolution [11]. From Harris' 1980 microscopy-based insight that cells deform a silicone substrate emerged a series of techniques – Traction Force Microscopy (TFM) and Micropillar Arrays – to map nanonewton scale forces at cell-substrate junctions with micrometer precision. By tracking the microscopic movements of fluorescent beads embedded within a gel, TFM can reconstruct force maps with micrometer precision and nanonewton scale [11, 12]. Other methods –optical and magnetic tweezers, atomic force microscopy, and biomembrane force probes– collectively deemed single molecule force spectroscopy

(SMFS), enable quantitation of force between single molecular interactions at piconewton scale [11]. A gap remained: neither technique could map the spatial distribution piconewton forces at cell-surface junctions.

Molecular tension sensors bridge this gap [11, 12]. By leverage the tension-mediated extension of a molecular linker to separate a fluorophore from a quencher, these tension sensors transduce force to an optical signal, and take several forms [13]. Genetically encoded tension sensors consist of a pair of suitable fluorescent proteins, capable of undergoing Forster Resonance Energy Transfer (FRET) when in proximity, separated by a linker, that can be inserted into a protein of interest. By measuring FRET levels one can infer tension [13-15]. Such sensors are uniquely capable of sensing intracellular forces. To measure forces receptors experience while interacting with the extracellular world, the Salaita lab developed a new series of tension sensors and pioneered a technique – molecular tension fluorescence microscopy (MTFM) – to visualize them [11, 12].

In MTFM, one end of a molecular tension sensor is immobilized to a surface, while the other presents a ligand specific for the receptor under study. Tension on this sensor extends the molecular linker, separating the fluorophore, typically a fluorescent dye, from a quencher, oftentimes another dye that can FRET quench the first, or perhaps a gold nanoparticle, leading to a turn-on signal [11, 12]. The first generation of probes employed entropic springs – disordered polymers such as PEG or some polypeptides – that extend gradually depending on force. While such sensors provide an analog response – the fluorophore's ensemble brightness varies smoothly with receptor force –quantifying cellular tension with this design is challenging, as a cluster of dim forces and a few bright forces are degenerate. To circumvent these issues, the lab developed DNA tension sensors that use a nucleic acid hairpin as the extensible element. Since hairpin folding and unfolding are highly cooperative, these sensors act digitally, opening in a narrow force range centered on $F_{1/2}$ – defined as the force at which a hairpin is equally likely to be found in open and closed states [11, 12, 16]. These nucleic acid-based sensors reveal whether force magnitudes exceed the $F_{1/2}$ threshold. (**Figure 1.1**.)

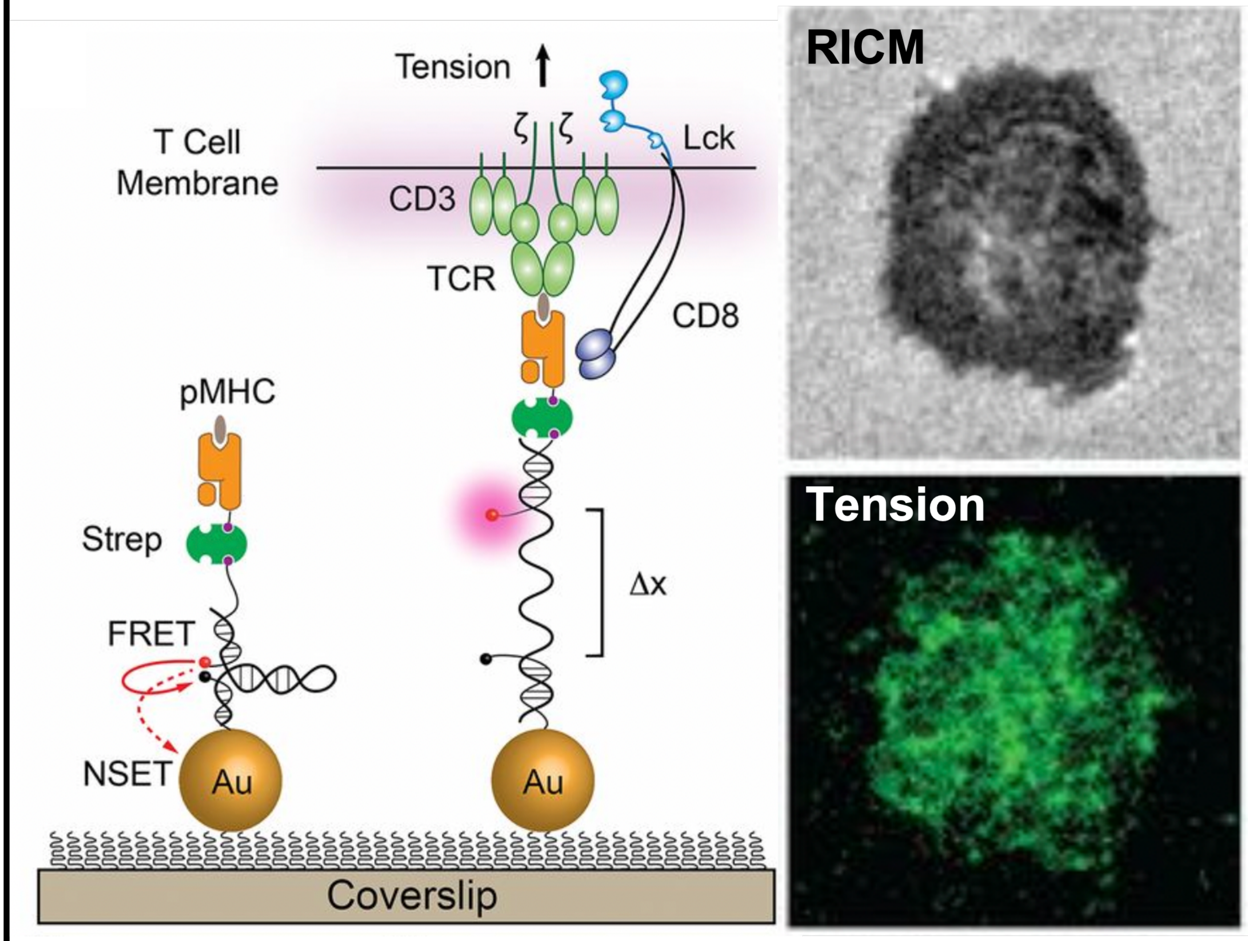

FIGURE 1.1: Molecular Tension Fluorescence Microscopy. Left: Schematic shows DNA hairpin-based tension sensor (black) attached to a surface via a gold nanoparticle (Au). Fluorophore (red dot) and quencher (black dot) in proximity for the closed hairpin. Quenching occurs by FRET and NSET (arrows). Tension on the hairpin attached ligand (pMHC) through a cellular receptor (TCR) separates the fluorophore from quencher by a distance (Δx), leading to fluorescence (red glow from fluorophore). Right: Upper image shows Reflection Interference Contrast Microscopy (RICM) image of T-cell spreading on a surface presenting an agonistic ligand, while the lower image shows a fluorescence map of the tension. Figure adapted from [1].

Nucleic acids' versatility has enabled the Salaita Lab to tune these hairpins. By changing the hairpin sequence and length, our group has engineered a library of hairpins with different force thresholds and has developed further variations on these designs to measure force orientations [17], track forces on fluid membranes [18, 19], capture transient forces [20], and map force's spatial distribution beyond the diffraction limit [21]. This proliferation of tools is essential for understanding biology; as Ham and colleagues note, cells sense more than force. Furthermore, cells are active, *responding* to surface mechanics; indeed, DNA nanotechnologies, such as tension gauge tethers, allow researchers to tune mechanical properties to probe their effect on cellular signaling [22, 23]. Disentangling mechanosensing mechanisms thus requires a deep understanding of the reciprocal relationships between probe structure, the physical parameters the probe transduces, the mechanical signature a probe provides a cell, and the cellular response.

This work seeks to take a step towards understanding mechanosensing by exploring these relationships. In the second chapter we seek to understand the effect of nucleic acid probe structure on its function. In the third chapter, I computationally explore a design to interrogate force lifetime – how long a mechanical bond sustains force. In the fourth chapter, we develop probes with unique mechanical signatures to explore the fundamental mechanisms of T-cell receptor triggering. The final chapter offers a brief conclusion.

Chapter 2: Understanding Tension Probe Structure and Function

This work was published in [24], and this chapter adapts from that paper.
Special acknowledgements to Dr. Roxanne Glazier and Dr. Hiroaki Ogasawara for their mentorship and essential contributions.

INTRODUCTION

While hairpin tension probe designs are generally conserved, different biological systems and questions demand subtly different mechanical and photophysical properties. By correlating the structural implications of two components – spacers and a donor-strand overhang – with spectroscopic and cellular data, we explore how subtle structural variations influence tension probe function. While possible, resolving multiple, high resolution tension probe structures was practically prohibitive. We thus turned to computational tools, stitching together a model from known NMR structures, then simulating this model with molecular dynamics to allow it to approach a more realistic form.

Molecular dynamics (MD) is a powerful theoretical approach for investigating biomolecular mechanisms and interactions that underpin biology that simulates, often in atomistic detail, the temporal evolution of a particular molecular structure. After calculating the forces on all the particles in a system at a given point in time, the MD algorithm uses Newton's laws to predict their positions and velocities a short time – usually a few femtoseconds – later. By repeating this process billions or even trillions of times, this algorithm can computationally simulate the motions of biomolecular structures on timescales approaching milliseconds. [25, 26]

To calculate these forces with speed and accuracy, MD algorithms employ force fields – simple mathematical approximations, informed by quantum calculation and experiment, of the energy of a given particle as a function of its charge, bond lengths, angles, dihedrals, and beyond. Accurate force fields are essential for accurate simulation. [26-28] This work employs the AMBERRNA forcefield, developed by Shaw and colleagues. [29]

Molecular dynamics is old: most of its groundwork was laid in the late 1960's and early 1970's, and it was first applied to a protein in 1977 [30]. Nevertheless, increased availability of protein structures, improved force fields, and exponential increases in computing power, have made molecular dynamics vastly more powerful and accessible, and contributed to its proliferation.[26, 27] Molecular dynamics enables us to better understand life in motion. In addition to improving structural predictions (as we do here), molecular dynamics has enabled researchers to peer into the mechanisms of transporters and ion channels, explore conformational changes induced by post-translational modifications such as phosphorylation, and find new sites for drug development. [26]

While extremely versatile, MD has limits. Being a classical-physics-based approximation, MD alone cannot simulate the formation or cleavage of chemical bonds, such as disulfides or protonation/deprotonations. Furthermore, the computational cost of simulating these systems limits simulation timescales: simulating a 50,000-particle system for a microsecond requires a few days of computing time on a single GPU. Ingenious software and hardware solutions – whether mixed methods protocols that integrate quantum mechanics with molecular dynamics or custom supercomputers designed for MD – have begun to address these challenges, though significant work remains. [25, 26]

This analysis was conducted using Yet Another Scientific Artificial Reality Application (YASARA), a powerful, comprehensive software package that enables turnkey simulation, molecular visualization, and straightforward analysis. [31, 32]

RESULTS

Here, we tested the effects of a three-nucleotide spacer and a five-nucleotide overhang on the stability of hairpin structures. The 3nt spacers fit between the arms and the stem-loop of the hairpin. The 5nt overhang attaches to the 3' end of the donor strand, which faces the three-way junction. We simulated all four combinations of spacer and overhang: no spacer, no overhang; no spacer, 5nt overhang; 3t spacer, no overhang; and 3t spacer, 5t overhang. (Figure 2.1.1) As the results below indicate, the three-way junctions (TWJ) of these four hairpins assume dramatically different conformations.

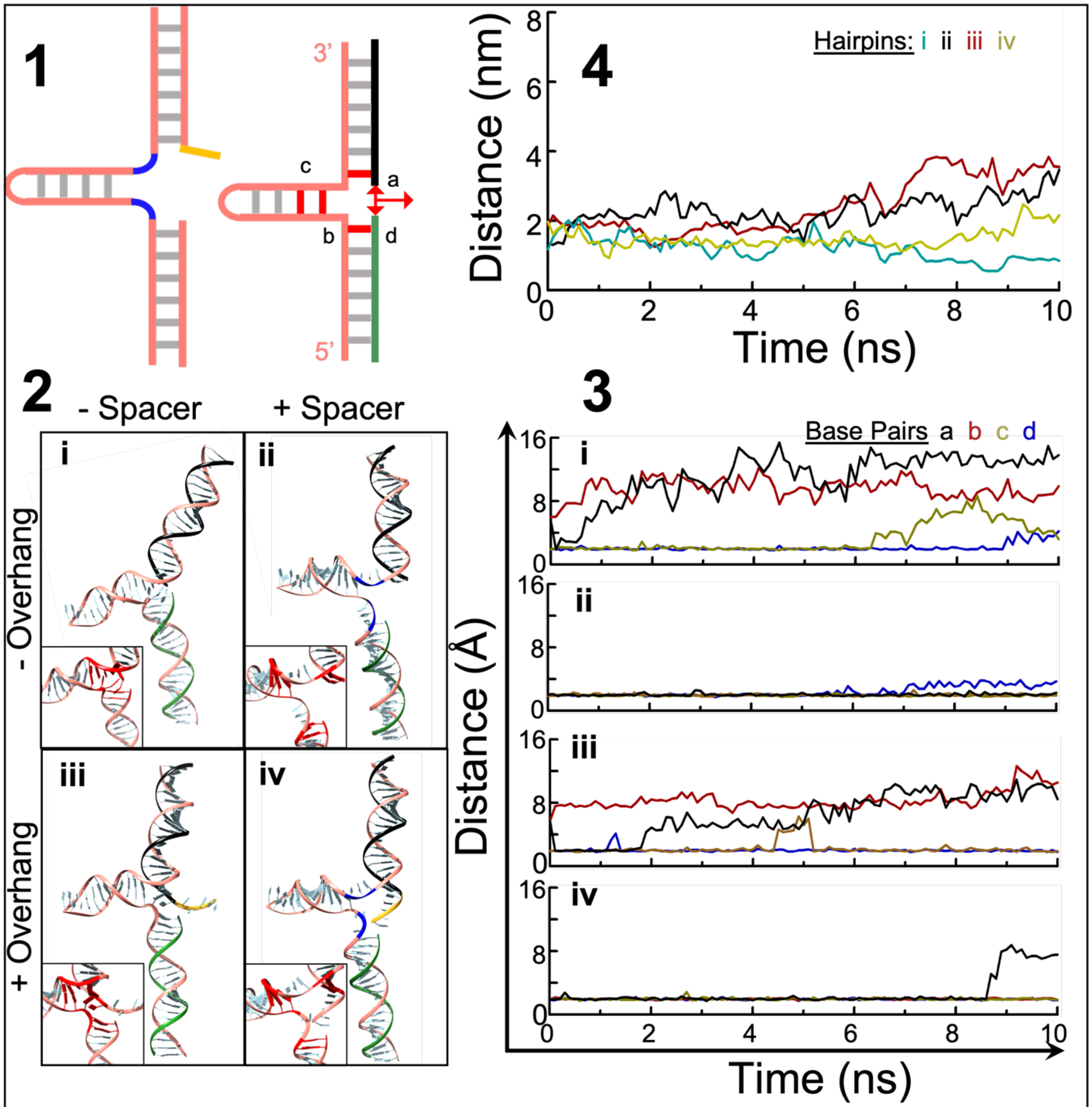

FIGURE 2.1: (1) Hairpin schematic depictions. Left illustrates the overhang (yellow) and spacers (blue) that change across hairpin structures. Right illustrates the nucleobase naming convention in the hairpin. Nucleobases a-d correspond to the traces listed in (3) and in future figures. The red arrow illustrates the distance calculated in (2). **(2) Hairpin structural depictions**. Representative resulting structures for the hairpins, illustrating effect of spacer and overhang on structure. Roman Numerals correspond to hairpins in (3). **(3) Time traces of base-pair hydrogen bonding face distances for hairpins.** These graphs illustrate representative time traces for the distances between hydrogen-bonding edges of the nucleobases for the base pairs a-d for hairpins i-iv. Each trace corresponds to a unique base pair; each graph corresponds to a unique hairpin. Low distances (~2 angstrom) suggest canonical, Watson-Crick hydrogen bonding, high distances suggest these hydrogen bonds are broken. Dramatic differences in stability are clearly visible. **(4) Time trace distance between fluorophore and quencher attachment sites.** Measuring the distance between fluorophore and quencher attachment sites (distance shown with red arrow in (1) helps us qualitatively predict the effects on quenching. Each trace corresponds to a different hairpin construct (i-iv).

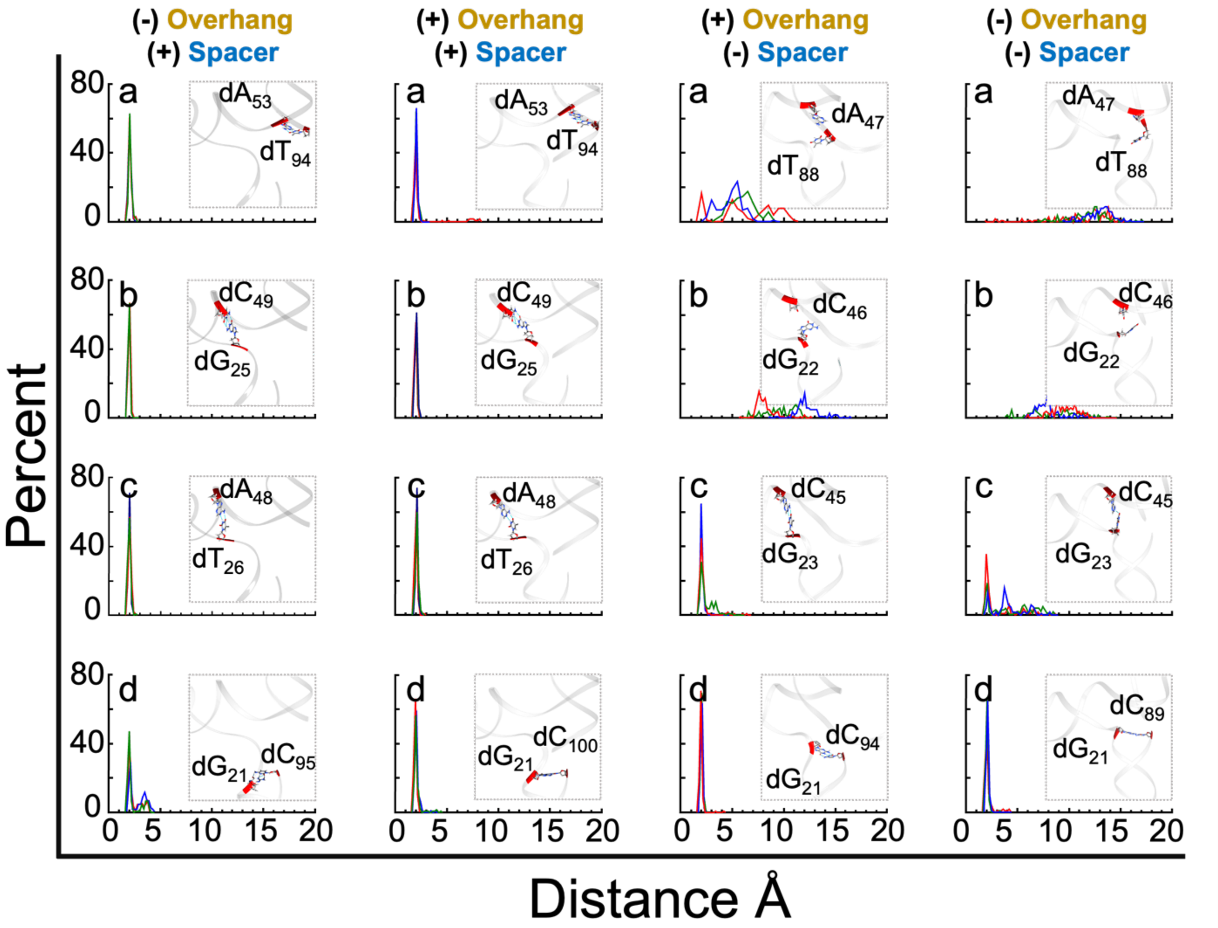

FIGURE 2.2: Base-pair distance histograms illustrate spacer-induced structural stabilization of TWJ-proximate nucleobases. Plotting a histogram of the distances between the hydrogen-bonding faces for nucleobase pairs labelled A-D enables estimation of the stability of hydrogen bonds: distributions strongly clustered around 2 Angstroms indicate the consistent presence of a hydrogen bond; distributions diverging strongly from this value suggest bond breakage. The red, blue, and green traces correspond to three different simulations from three slightly different starting positions. Inset images illustrate the TWJ structure, with the base-pair whose distance is being measured by the histogram colored in red. Histograms are arranged in column by the hairpin construct and in rows by the base pair. Comparing the first two columns with the last two columns suggests that spacer removal destabilizes most junction-proximate base pairs (except D). Comparing constructs with overhangs to those without them suggests a slight stabilization effect, as observed by distances.

+ Spacer Hairpins

The standard hairpin (with a 3T spacer and lacking a 5T overhang) displays an open TWJ with no intruding nucleobases and clean Watson-Crick base pairing at the three ends of the duplexes. An added 5T overhang to the donor strand stacks helically on itself, narrowing the gap between donor and acceptor strands without significantly altering the TWJ's hydrogen-bonding pattern. (Figure 2.1.2) Examining the distances between the hydrogen-bonding edges of the nucleobases surrounding the junction sharpens this insight. A time-trace of these distances reveal few deviations from ~2 angstroms, supporting the conclusion that these nucleobases are generally stably hydrogen-bonded. (Figure 2.1.3)

The + Overhang and - Overhang hairpins display subtle differences. For the + Spacer, + Overhang construct, base pair a appears to suddenly assume a separated conformation at the end of the simulation, but base pair D is stable. In contrast, for the + Spacer, - Overhang construct, base pair D in displays a slight increase in distance as the simulation extends, as if breathing. (Figure 2.1.3) Histograms of the distances of these base pairs for three different runs suggest base pair A's conformational switch wasn't observed in the replicate runs of the +Spacer, +Overhang hairpin, while base pair D spends a significant portion of time in the frayed state for the + Spacer, - Overhang hairpin. (Figure 2.2)

That base pair D, a GC interaction, frays in the + Spacer, -Overhang structure is somewhat counterintuitive, especially as its counterpart on the other edge of the TWJ, base pair A, an AT interaction, shows no such behavior. However, the addition of the 5T overhang appears to suppress this breathing, perhaps by adding a stabilizing pi-stacking interaction or through some other steric effect– thus this fraying is not seen in the +Spacer, +Overhang hairpin. (Figure 2.1.3, Figure 2.2).

Closer examination of the +Spacer, +Overhang hairpin suggests that the flexibility of the upper 3T linker may be impaired by the addition of the 5T overhang; this may concentrate stress on nucleobase A and help increase the likelihood that nucleobase A breaks, relative to the +Spacer, -Overhang construct. (Figure 2.1.2) Nevertheless this change is still unlikely and thus isn't recapitulated in other runs. (Figure 2.2)

- Spacer Hairpins

Contrasting with their spaced-out counterparts, the hairpins lacking spacers demonstrate much greater structural disruption. Lacking spacers, the - Spacer, - Overhang TWJ changes – formerly well-behaved base pairs break, and their constituent nucleobases intrude into the junction, crowding it. (Figure 2.1.2). The time traces of distances between the hydrogen bonding faces of the proximal nucleobases shows marked deviation from the ~2 angstrom baseline: nucleobases A and B are extremely disrupted, and C is moderately so. (Figure 2.2) The structural models are illuminating: removal of the spacer increases the local curvature of the backbone: whereas the spaced-out backbone uses five nucleobases to make a 90-degree turn, the spacer-less backbone has just two nucleobases. This sharp turn concentrates strain into beginning nucleobase of the hairpin (nucleobases B and C). Furthermore, this strain appears to interact with duplex's helicity to break base pair A. To minimize this curvature induced stress, the entire model assumes a noticeably bent conformation.

The inclusion of the 5nt overhang in the - Spacer, + Overhang construct appears to conformationally lock the TWJ. As if a door wedge, this overhang untwists the hairpin helix ever so slightly and pries the backbones apart, as if a door wedge, enabling the second base pair of the hairpin (base pair C) to reform. Simultaneously, the first base pair (B) of the hairpin is twisted out into the middle of the junction, slightly closer to its hydrogen bonding partner though still unable to interact. Finally, the base pair prior to the junction, nucleobase A, is also locked closer to its hydrogen bonding partner, though again it is well outside the hydrogen-bonding distance. The time traces and histograms support this assessment. The absolute magnitudes of the deviations from baseline in the time traces are less for the -Spacer, + Overhang hairpin than with the - Spacer, - Overhang hairpin. The histograms for nucleobase A reveal distances closer to the hydrogen bond length for the - Spacer, + Overhang hairpin versus the - Spacer, - Overhang construct, while the histogram for base pair C suggests it spends a greater proportion of time in the bonded state for the - Spacer, + Overhang hairpin over the - Spacer, - Overhang hairpin. Finally, this steric crowding prevents the overhang from stacking helically as it had in the + Spacer, + Overhang case – instead it sticks out from the junction. Removing spacers thus crowds the junction and disrupts the structure, though addition of the 5T spacer appears to stabilize some fraying bases by sterically jamming them into place.

DISCUSSION

Effect of Structure on Mechanics

While our three-way junction's nicked structure precludes direct comparison with much of the existing TWJ-structure literature, one can carefully draw useful parallels. As Glazier noted: Welch and colleagues' electrophoretic analysis of bulge sequences concluded that strain precludes perfect three-way junctions from coaxially stacking, and these models suggest nick in this structure doesn't abrogate this effect. Welch adds that spacing the junction through the addition of bulge nucleotides enables coaxial stacking of two of the helical arms. [24, 33] We observe a related effect: spacer addition relieves strain and (generally) promotes coaxial stacking of the terminal bases *within* the three arms, but our model does not support coaxial stacking *between* helical arms. This latter discrepancy likely arises from the differences in the secondary structures of these TWJ's: Welch's constructs lacked the three-nucleobase spacers, keeping the hairpins more proximate and likely enabling this stacking.

While secondary structure variations significantly alter the three-way junction geometry, these effects are unlikely to significantly affect the system's mechanobiology. Woodside and colleagues note that the termini of folded nucleic acid hairpin fray by approximately 1-2 nucleobases. [16] Our models recapitulate this fraying only in spacer-less hairpins. Given that the starting positions lacked fraying and that a 10-nanosecond simulation is unable to sample the entire conformational space (or, more succinctly, it isn't ergodic), these data suggest that the spacer-less hairpins are strongly driven towards a frayed state, while the spaced-out hairpins are driven less so. Using an energy landscape model developed by Woodside, Glazier calculated the difference in $F_{1/2}$ – the force at which the free energies of closed and opened states are equivalent – between unfrayed and 2-nucleobase frayed sequences: 1.3 pN. While numerically significant relative to the $F_{1/2}$ values (~5 pN), we argue this difference is likely biologically insignificant: in a system imaging integrin tension on supported lipid bilayers, no changes in signal underneath cells were observed between spaced-out and spacer-less hairpins, suggesting no biological effect for this system. [24] While the absence of a biological effect for integrins – receptors known to deliver relatively high forces [22] – may not generalize to lower-force receptors, the $F_{1/2}$ of these probes depends significantly on buffer conditions, with various single molecule force spectroscopy experiments on the same hairpin yielding values from 4.7 to 7.8 pN. Since the mechanical implications of spacer deletion are well within this range, spacer deletion is unlikely to be useful as a tool to fine-tune the tension threshold. However, the difference in stability may be significant for non-mechanical reasons: the induced fraying may both subtly accelerate strand dissociation kinetics, which can become relevant for long experiments, while potentially increasing susceptibility to nuclease degradation.

Structure and Photophysics

The model accurately predicts the qualitative effects of spacers on fluorophore-quencher distance in probes lacking overhangs. For probes lacking overhangs, Glazier's fluorescence data suggests that removing spacers increases the quenching efficiency for Alexa488/Cy3B probes, indicating the gap between fluorophore and quencher decreases. While no significant change in quenching efficiency occurred for A488/BHQ and Cy3B/BHQ quenched probes, both these probes were very highly quenched (98-99%), possibly rendering the change immeasurable. Indeed, changing the quencher attachment point, from the terminus abutting the TWJ to a point on the DNA backbone 9 nucleotides from the donor, resulted in a decreased QE for both A488/BHQ and Cy3B/BHQ pairs. [24] This aligns with the model, in which removing spacers increases the proximity between the quencher and donor attachment points. As illustrated in Figure 2.1.4, the distance between the fluorophore and quencher attachment points is lower for the -

Spacer, - Overhang construct (hairpin i) than for the + Spacer, - Overhang construct (hairpin ii), as the simulation goes on.

In contrast, the model struggles to accurately predict the effect of a 5 nt overhang. Except for the spacer-less Cy3B/BHQ design, where no significant change in quenching efficiency is observed, addition of the overhang leads decreases the quenching efficiency by separating the fluorophore with the quencher. Spectroscopic analysis of the Cy3B/BHQ designs implicate static quenching, implying that fluorophore and quencher are touching. We hypothesize the extended linker structure of the Cy3B enables it to contact the BHQ despite the overhang's added length [24]. The model's predictions are more complex: for spacer-less probes, the overhang distends away from the three-way junction and should increase the distance between fluorophore and quencher (Figure 2.1.2, 2.1.4 Hairpin iii). Barring the previously discussed Cy3B/BHQ case, these predictions are borne out: the overhang decreases the quenching efficiency of A488/BHQ and A488/Cy3B probes. For probes with spacers, by contrast, the model predicts that the overhang helically stacks upon itself to bring the fluorophore and quencher attachment points closer together (Figure 2.1.2, 2.1.4, Hairpin iv). This is refuted by the data – all spaced designs display decreased quenching with overhang addition. This consistent error suggests two effects. First, since the simulations are not ergodic, the hairpins haven't covered their entire conformational space. Since the overhangs were helically stacked in the starting model, this stacking will likely remain absent a strong thermodynamic preference against this position (as observed in the + Spacer, + Overhang structure). Second, the dye-dye interactions may make important unseen structural contributions. As Glazier notes, dye-quencher interactions are known to alter melting curves, and these may preferentially stabilize certain hairpin conformations over others. [24].

CONCLUSIONS AND NEXT STEPS

These data suggest that probe three-way junction structures are highly sensitive to probe sequence and begin to provide a mechanistic explanation for the increase in quenching upon spacer removal and the increase in quenching upon spacer removal and 5nt overhang addition. While these structural differences affect photophysics, they do not significantly affect mechanics.

The discussion illuminates these simulations' most significant caveat: they lack dyes. Simulating dyes is challenging – as Graen and colleagues note, a dearth of experimental data combined with these dyes' polarizable, extensively delocalized structures complicates efforts to develop accurate force-field parametrizations. While recent work has begun improving in this regard– Graen and colleagues developed the AMBER-DYES force field for 22 common fluorophores, while Best *et al* optimized force field parameters for Alexa Fluor 488 and 594 to quantitatively predict FRET transfer efficiencies across a polyproline helix – they were, unfortunately, lacking for key components of our system. [34, 35] Only one of our dyes had an explicit parametrization (Alexa488) within the AMBER-DYES set.[1] While an all-*trans* conformation of Cy3 was included in the set (paralleling Cy3B, absent the rigidifying alkane linkers), no chromophore like BHQ was present. Absent these refined parameters, we neglected the dyes, simplifying the

---

[1] Cy3B wasn't in the set, though an only all-trans form of Cy3 (a non-rigidified form of Cy3B) was.

simulation’s execution and interpretation (data is only as good as the assumptions grounding it). However, future work could include dyes. Additionally, some fluorescence data suggested these structural models’ validity may be constrained by the relatively small sample space the molecules traversed in 10 nanoseconds. More sophisticated, enhanced sampling techniques [36], either alone or in conjunction with longer simulation times, could improve the scope of the conformational space probed by these hairpins. Further simulations could also computationally add forces to the hairpins, thereby probing the effects of these structural disruptions on tension probes’ force-extension curves and $F_{1/2}$ values, either through coarse-grained packages (like oxDNA [37]) or in full atomistic detail.

METHODS

All hairpins probes were modeled in YASARA [31] and visualized in Chimera [38]. Following cell neutralization [39], YASARA simulation was performed atomistically for 10 ns under an isothermal−isobaric ensemble with the AMBER RNA force field. [29] Simulations used a cutoff of 8 Å and a timestep of 2.5 fs. The models employed an improved Berendsen Thermostat [40] and a particle mesh Ewald [41]. Simulation conditions were conducted with periodic boundaries at 0.9% NaCl (w/v), pH 7.4, 298 K, and at atmospheric pressure. Water was filled to a density of 0.997 g/mL and was modeled with a TIP3P equivalent.

The tension probes were constructed in pieces using existing experimentally verified structures. The 20 nt duplex arms were created through in silico mutation of an NMR-acquired structure of a 21 bp DNA duplex (PDB: 2JYK) [42]. The hairpin portion was based off an NMR-acquired structure of a 27 nt AT-rich hairpin with a 3T loop (PDB:

1JVE) and was modified in silico [43]. The models were relaxed in an incremental fashion to maintain a reasonable structure and then were ligated with the 3T spacers flanking the stem−loop. The final probe structure with the spacers was then produced by stepwise relaxation. To produce the final probe lacking spacers, the 3T loops were excised from the standard hairpin strand and the structure again was relaxed in a stepwise fashion. 5T overhangs were added in YASARA to both structures, and their addition was followed by a stepwise relaxation to produce D probes containing a 5T overhang at the 3′ terminus of the donor strand.

For each simulation frame, the distances between the C1 atoms of the ends of the duplexes facing the hairpin were calculated. The distances between the nucleobase hydrogen bond donors and their acceptor partners were calculated for each nucleobase surrounding the duplex/hairpin junction and were averaged to produce a distance for each nucleobase. Molecular dynamics simulations were conducted in triplicate. To minimize the role of starting conformations on simulation outcome, starting structures for the replicate simulations were obtained through energy minimization of the structure captured at 3.3 ns of the previous replicate; the random number seed was also changed, and the simulation rerun under otherwise identical conditions.

Chapter 3: Mathematically Modeling Probes to Measure Bond Lifetime

Special Acknowledgement to Dr. Aaron Blanchard for insights into developing the mathematical model used here.

INTRODUCTION

“Catch bonds” – interactions whose lifetime increases under force – represent an intriguing and multifunctional mechanobiological adaptation. While most biochemical interactions form slip bonds, which weaken under tension, certain macromolecular interactions do the opposite, strengthening under tension like flexible finger-trap toys. First theorized in 1988 by Dembo and colleagues, the catch bond was experimentally found in 2003 in the leukocyte p-selectin’s interaction with PSGL1 and has since resurfaced across biological systems and contexts [44]: filamentous actin-myosin complexes [44], bacterial cellulosomes [45], leukocyte l-selectin interactions (where it mediates leukocyte rolling) [43], the SARS-CoV2 Spike/ACE-2 complex (where the catch bond may mediate infectivity) [46]. Perhaps most intriguingly, catch bonds may mediate antigen recognition by T-cells [2, 47-49]. This range suggests catch bonds may be a general biological mechanism, and thus developing mechanobiological tools to understand catch-bonds is essential.

“Catching” a catch bond requires ascertaining a bond lifetime under force, often with single-molecule force spectroscopy: optical-tweezer-, magnetic-tweezer-, biomembrane-force-probe-, or atomic-force-microscope-based assays [2]. While powerful, these techniques can only measure a few bonds at a time. Developing a luminescent tension probe to map bond lifetime with nanometer resolution underneath a cell would open another dimension of scientific inquiry by allowing us to examine the spatiotemporal evolution of catch bond behavior in biological contexts.

Such a luminescent probe requires an optically detectable process both exclusive to probes under tension and whose lifetime approximates that of the bonds we seek to interrogate, which, for T-cells, is measured in seconds [47-49]. This optically detectable process would begin upon probe opening, and the expected ensemble optical signal would increase at a rate dependent on the process lifetime. Upon probe closing, the process would end, and the optical signal would drop. At mechanical steady state (where the number of open probes is constant over time), this readout would reach a value that is a function of both optical process and bond lifetimes. Equipped with the process lifetime, the experimenter could simply calculate the bond lifetime.

Multiple suitable optically detectable processes exist. In soon-to-be-published work, Rong Ma and colleagues deploy the binding kinetics of a single-stranded DNA to lock open tension probes at a well-defined rate; through a series of such experiments, they estimate the bond lifetime of a variety of T-Cell Receptor/Peptide MHC interactions. Inspired by their idea, I asked whether long-lifetime luminescence can be used to measure the bond lifetime.

Here, long-lifetime luminescence refers to a process resulting in the slow reemission of light upon illumination. By slowing the transition rate between the excited and ground states of a system, often through stabilizing triplet states and excitons, [50, 51] long-lifetime luminescence processes can span timescales from microseconds [52] to hours and beyond. [50, 51] Fluorescence, in comparison, generally occurs within nanoseconds. Their unique emissive properties contributes to long-lifetime luminophores' increasing use in biological settings: Oxygen-quenched phosphorescent dyes can optically transduce oxygen levels [53]; long-lifetime lanthanide emitters have been combined with time-gating imaging techniques to form ultrasensitive luminescent molecular tags [52]; ultralong afterglow luminescent nanoparticles have been proposed for in-vivo imaging [54], while upconverting nanoparticles have been investigated for anticancer applications [50, 53]. To date, however, long-lifetime luminophores have not been used to investigate bond lifetimes.

Probe Design

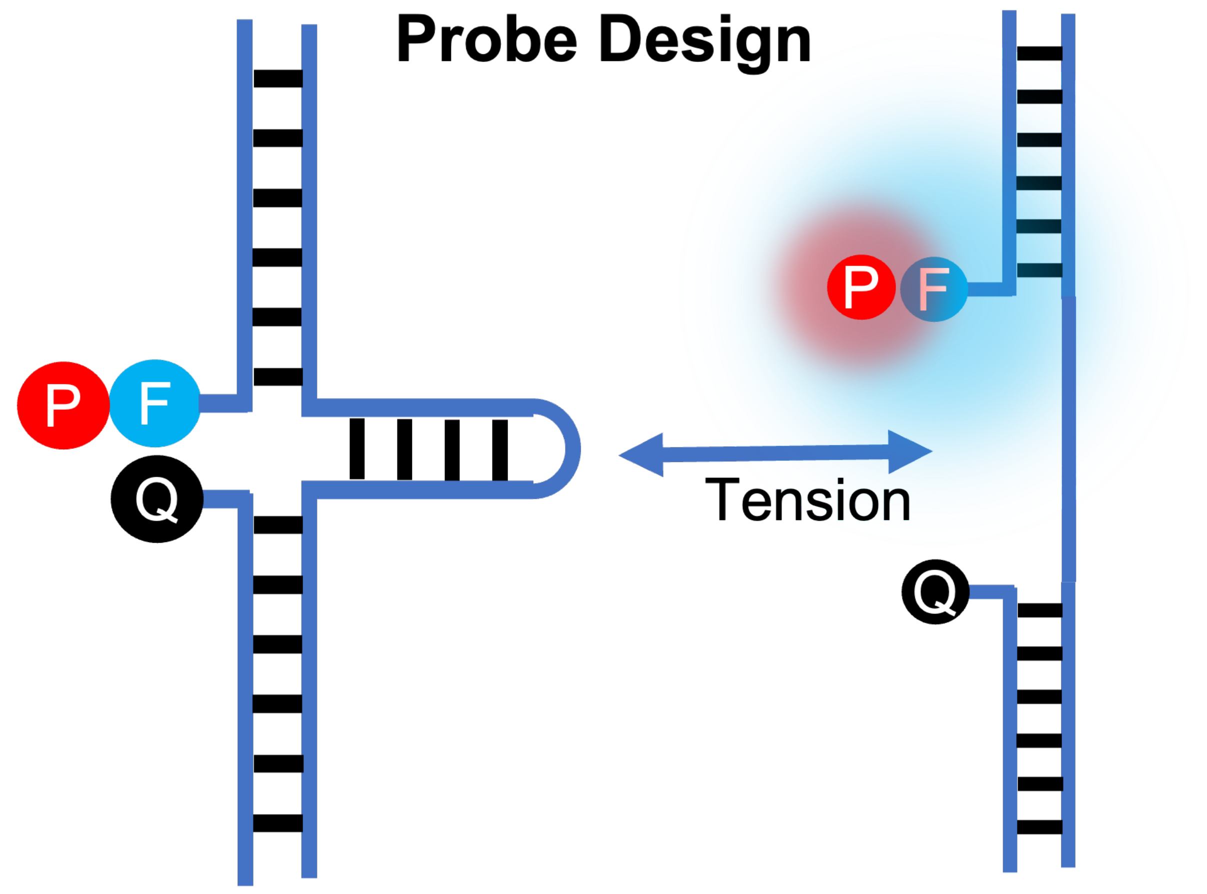

FIGURE 3.1: Ratiometric Lifetime Sensing Probe. This design evolves the standard tension probe by a phosphor (P), in addition to the fluorophore (F) and quencher (Q). Under tension these luminophores separate leading to emission. The ensemble phosphor intensity hinges on the ratio of the phosphor and bond lifetime.

The initial probe design called for a fluorophore, a phosphor, and a quencher situated at a three-way junction, illustrated in **Figure 3.1**. Upon probe opening, the now-unquenched fluorophore would rapidly be excited by an incoming photon. This energy could be rapidly re-emitted through fluorescence (as with the standard tension probe designs) or could excite the phosphor. If the excited phosphor transitioned to its ground state prior to probe closing, it's energy would be emitted as light; If the probe closed, however, the phosphor would drain its energy through the quencher and remain dark. Short force lifetimes would cause more such premature closure, suppressing the phosphorescent signal, while long force lifetimes would enable more phosphors to shine, enhancing the phosphorescent signal. Since system fluorescence indicates the number of open probes, ratiometric comparison of fluorescence with phosphorescence would allow bond lifetime measurement.

Mathematical Model Derivation

To interrogate this system's viability by identifying requisite phosphor lifetimes and predicting photon counts, I constructed a kinetic model, shown in **Figure 3.2**. At Dr. Aaron Blanchard's suggestion, I neglected the fluorophore, instead focusing exclusively on the phosphor. This system has two independent components with two states each – the luminophore, which exists in a ground or excited form, and the hairpin, which exists in an open or closed form. There are thus four independent states: closed hairpin, ground-state luminophore **(CG)**; open hairpin, ground-state luminophore **(OG)**; closed hairpin, excited-state luminophore **(CE)**; and open hairpin, excited state luminophore **(OE)**.

By assuming first-order kinetics, that the photophysics doesn't influence cellular mechanics, and that only one component (hairpin mechanical state or luminophore electronic state) changes at a given time, we derive that the hairpin-closing rates are: $k_{close}[OE]$ and $k_{close}[OG]$ for hairpins with excited and ground-state luminophores, respectively, where k_{close} is some rate constant. Similarly, the reverse transitions (from closed to open) can be expressed as $k_{open}[CE]$ and $k_{open}[CG]$ for excited and ground-state probes, respectively.

Similar equations describe the interconversion of luminophore electronic states. Assuming first order kinetics, the luminophore excitation rates can be written as $k_{excitation}[CG]$ and $k_{excitation}[OG]$, for closed and open hairpins respectively. The reverse process includes quenching and emission and assumes different forms for open and closed hairpins. To simplify the mathematics, we assume that quenching both purely dynamic and is negligible in open probes. Thus, the rate of de-excitation for open hairpins appears: $k_{emission}[OE]$. Including quenching effects, the rate of de-excitation for closed hairpins takes the form $k_{emission}[CE] + k_{quench}[CE]$.

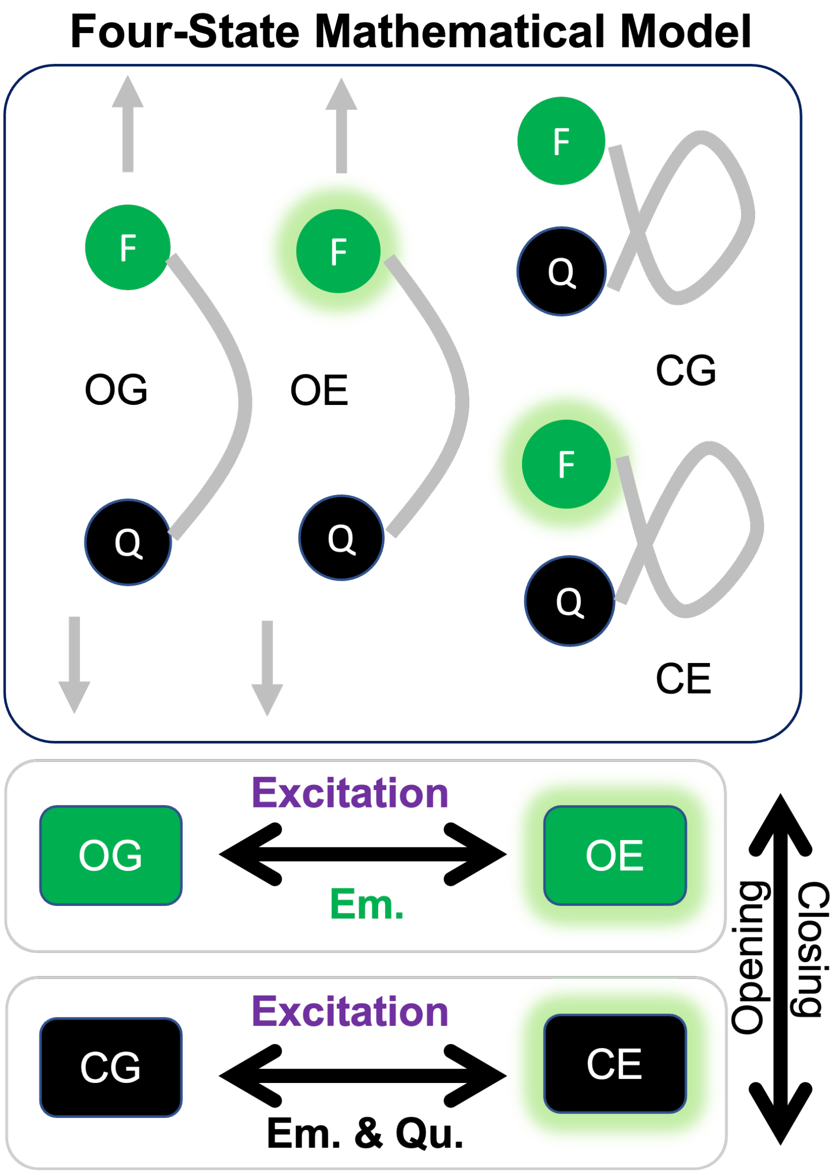

FIGURE 3.2: Derivation of mathematical model. Top pane depicts the four mechanical states the model considers: Open, Ground (OG); Open, Excited (OE); Closed, Ground (CG) and Closed, Excited (CE). Grey arrows indicate the tension that separates fluorophore and quencher in the open states. Bottom Pane shows the processes that allow probes to transform between these states: excitation, emission (Em.), quenching (Qu.), opening and closing. We assume no two processes occur simultaneously.

We can thus construct a system of four linear, ordinary differential equations that capture the system's behavior over time:

$$\frac{d}{dt}[CG] = k_{close}[OG] + \left(k_{quench} + k_{emission}\right)[CE] - \left(k_{open} + k_{excitation}\right)[CG] \tag{1}$$

$$\frac{d}{dt}[OG] = k_{open}[CG] + k_{emission}[OE] - (k_{close} + k_{excitation})[OG] \tag{2}$$

$$\frac{d}{dt}[CE] = k_{close}[OE] + k_{excitation}[CG] - \left(k_{open} + k_{quench} + k_{emission}\right)[CE] \tag{3}$$

$$\frac{d}{dt}[OE] = k_{open}[CE] + k_{excitation}[OG] - (k_{close} + k_{emission})[OE] \tag{4}$$

Yet most of these rate constants are neither directly observable nor tunable and must be calculated from other parameters.

We define:

$$k_{close} = \frac{1}{\tau_{force}} \tag{5}$$

Where the denominator (tau-force) is the force lifetime we seek to measure. From this we can infer the opening rate as a function of the percentage of open probes:

$$k_{open} = \frac{p_{open}}{1 - p_{open}} k_{close} \tag{6}$$

Where p_{open} is the proportion of open probes underneath a cell. For this analysis, we estimate it at 10%.

The expressions for the emission and quenching rates assume similar physiognomy:

$$k_{emission} = \frac{1}{\tau_{emission}} \tag{7}$$

$$k_{quench} = \frac{QE}{1 - QE}\, k_{emission} \tag{8}$$

Where again, tau-emission is the lifetime of the luminophore, and QE is the quenching efficiency of the probe in the closed state. From Glazier, *et al* we assume a quenching efficiency of 0.9 [24].

The remaining kinetic value, $k_{excitation}$, depends on both the photon density of the illumination and the absorption cross-section of the luminophore, which, in turn, depends on the extinction coefficient [55]:

$$k_{excitation} = \left(\frac{P}{A}\right)\left(\frac{\lambda}{hc}\right)\left(\frac{\epsilon * \ln(10) * 10^3}{N_A}\right) \tag{9}$$

Where P is the illumination power (in mW), A is the objective area through which that illumination is focused (in square microns), λ is the wavelength, h and c are Planck's constant and the speed of light, respectively, ε is the extinction coefficient, and N_A is Avogadro's number. The standard illumination is estimated at 1 mW (approximately the illumination power of the laser sources in TIRF imaging, while the objective area is 100 sq. µm.

Finally, the photon emission rate is:

$$Emission = [State] * \Phi * \rho * A \tag{10}$$

Where ϕ is the quantum efficiency, ρ is the surface density, and A is the area of the objective. If [State] corresponds to an open, excited state, then this equation yields the signal photon emission rate – the rate of emission from opened probes. If [state] corresponds to a closed, excited state, then this equation yields the background photon emission rate – the emission rate from closed probes.

The values employed are summarized here. The value the probe seeks to measure – the bond lifetime, is highlighted in green. The parameters I manipulated to measure that lifetime are highlighted in orange.

Component	Parameter (Symbol: Unit)	Value	Notes
Dye	Mol. Ext. Coeff (ε: M^{-1} cm^{-1})	130000	Cy3B [56]
Dye	Excitation Wavelength (λ: nm)	560	CY3B
Dye	Lifetime (τ: ns)	**Varied**	2.5 ns for Cy3B
Dye	Quantum Yield (Φ)	0.67	Cy3B
Surface	Probe Density (ρ: μm^{-2})	2000	From [21]
Surface	Quenching Efficiency (QE)	0.9	From [24]
Surface	Open Probe Prop. (p_{open})	0.1	Estimate
Microscope	Objective Area (A: μm^2)	100	
Microscope	Laser Power (P: mW)	**Varied**	1 mW typical
Simulation	Timestep (ps)	10	
Simulation	Queue	10	Varied later to improve numerical stability. See below.
Simulation	Steady State Deviation (%/s)	0.01	The threshold for change below which the simulation is considered to be at steady state. This deviation is calculated by measuring the change in value of a given proportion over a queue (see above) of the most recent simulation values, then scaling appropriately.
Cell	**Force Lifetime (s)**	**0.001 - 10**	**What I seek to measure**

In addition to luminophore lifetime, I also probed illumination intensity as a potentially tunable parameter. Since the lifetime of a luminophore's ground state decreases as illumination intensity increases, I reasoned that manipulating the illumination intensity to bring the ground state lifetime close to the bond lifetime may achieve a similar effect as altering the luminophore excited state lifetime. The ground state lifetime is simply the inverse of the excitation rate:

$$\tau_{excitation} = \frac{1}{k_{excitation}} = \left(\frac{1}{\left(\frac{P}{A}\right)\left(\frac{\lambda}{hc}\right)\left(\frac{\epsilon * \ln(10) * 10^3}{N_A}\right)} \right)$$

For the parameters listed above, this ground-state lifetime is ~71 μs.

The steady state solution of this system of differential equations yields the proportion of probes in each population, from which we can infer signal and background photon counts for each set of probe and system parameters for a given bond lifetime. To understand the probe's responsiveness to the bond lifetime, I calculated the dynamic range across four orders of magnitude of force lifetimes – from 1 millisecond to 10 seconds.

The specific question now comes into focus: Can one manipulate the luminophore lifetime or the illumination intensity to produce a usable dynamic range?

"Usable dynamic range" is an intentionally vague term, but comparisons are helpful. An ideal sensor would display no signal in an off-form and full signal in an on-form. If we normalize to the on-signal, then the dynamic range is 1. By themselves, the lab's standard digital tension sensors are approximately 95% quenched in the closed state [11]. If we normalize the open-state signal as 1, this corresponds to a dynamic range of 0.95. Analog tension sensors have a dynamic range of approximately 0.7 [11].

If the answer is affirmative, then we ask the following:

1. What luminophore lifetime or illumination intensity optimizes the dynamic range?
2. What is the expected signal-to-background ratio of these probes?
3. What photon counts would we expect from these probes?

While an analytical solution for this system may exist, I pursued a straightforward numerical approach: Euler's method. At each step, the code calculates the rate of change of each population of probes based on the others. The code then linearly interpolates this change out for a small timestep (generally 10 ps) before recalculating the derivatives. This process is repeated until the code hits a steady state condition, defined as a proportional change of less than 0.1%/second for 10 consecutive readings. At steady state, the code derives the predicted photon fluxes, from which dynamic range and signal-to-noise can be calculated.

RESULTS

Model Stability

To verify the code's stability, I ran the simulation predicting the steady-state population values from a fully open CY3B-labelled surface (**Figure 3.3**). The relevant parameters were as follows:

Component	Parameter	Value	Notes

Dye	Lifetime (ns)	2.5	Cy3B Lifetime
Microscope	Laser power (mW)	1	Default
Surface	Open Proportion	1	Fully Open Surface

Plotting the proportion of probes in excited and ground states over time yields a curve that stabilizes after ~50 ns, suggesting that the code, as implemented, is stable.

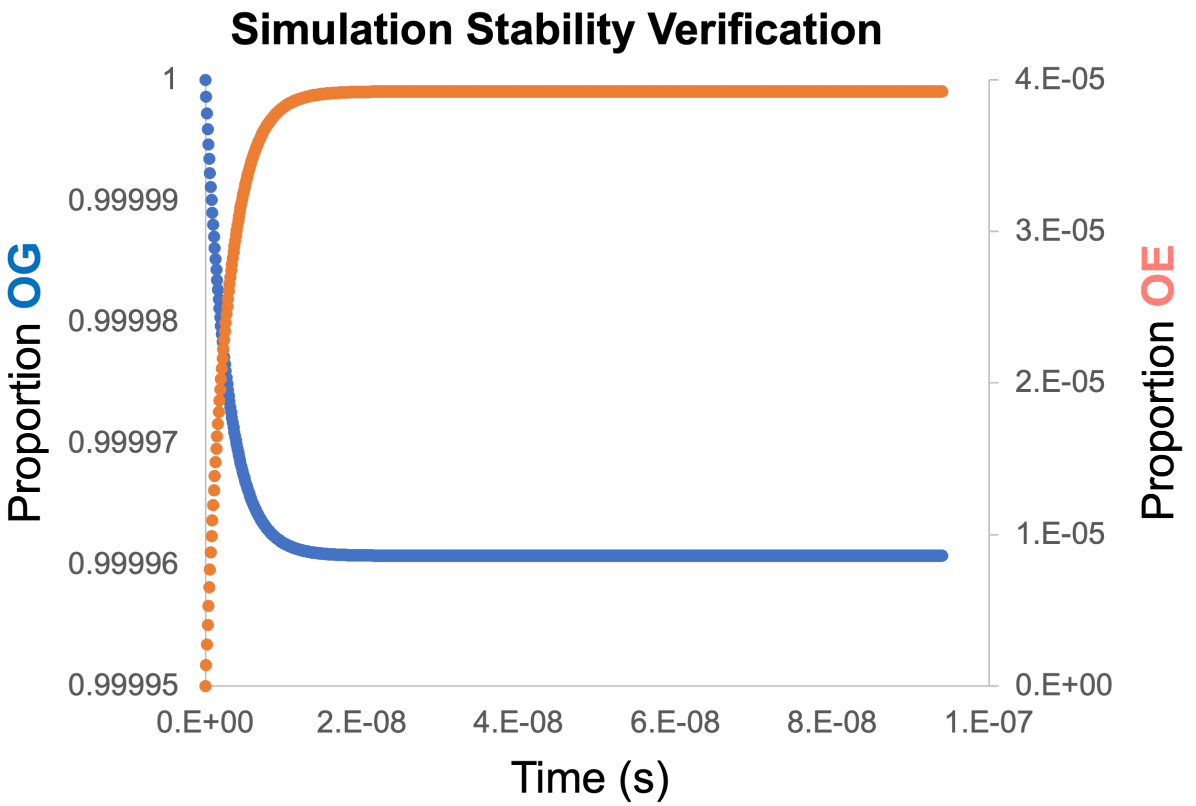

FIGURE 3.3: Simulation Steady State Stability. Predicting the proportion of excited and ground-state probes for a fully open surface labelled with Cy3B demonstrates a quick approach to steady state, suggesting the model's computational implementation is stable. **Orange** trace corresponds with Open, Excited (**OE**) state. **Blue** trace corresponds to Open, Ground (**OG**) state.

Excitation Intensity

I next tested nine orders of magnitude of excitation powers to ascertain whether excitation intensity could reveal bond lifetime. Plotting the normalized photon counts for each excitation intensity (defined as photon count for an individual point in a trace divided by the average photon count for all points in the trace) as a function of bond lifetime yielded no correlations, suggesting no effect. Major fluctuations for low-intensity traces suggest numerical instability.

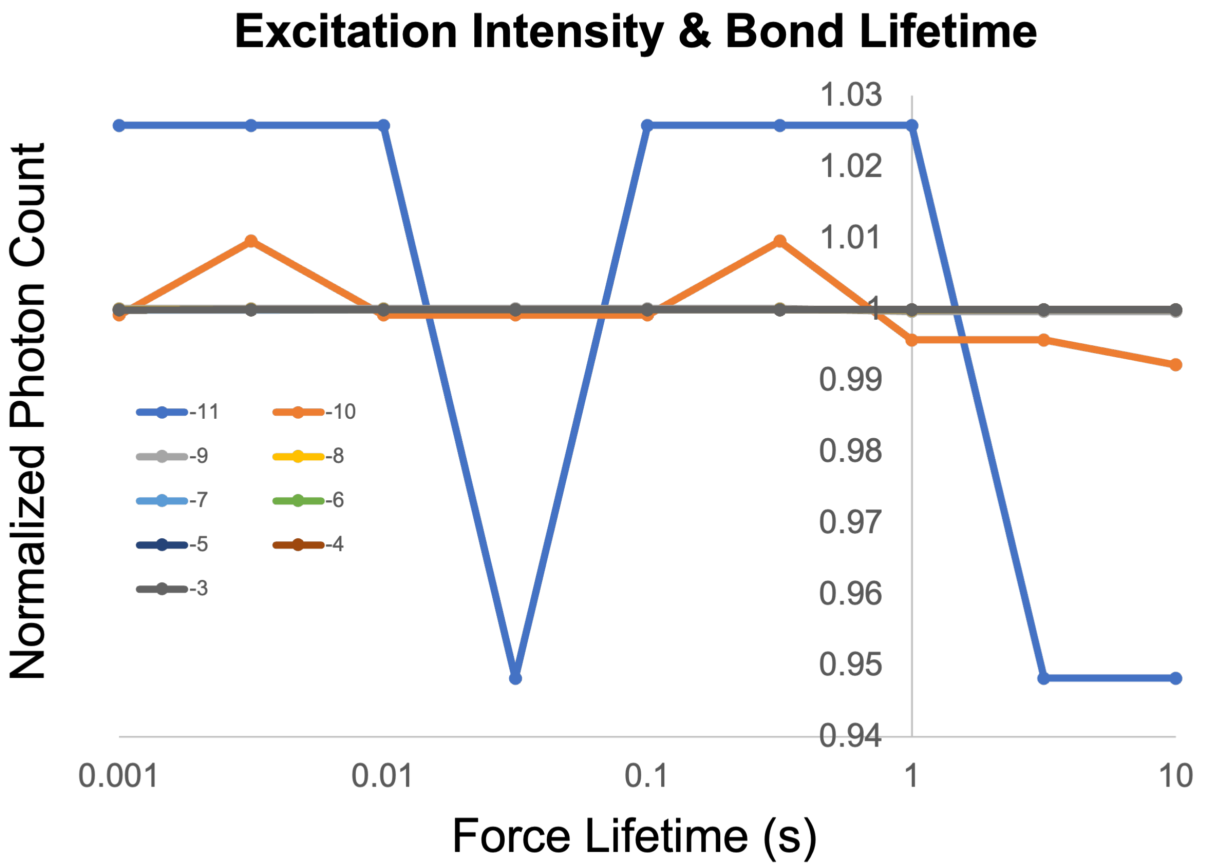

FIGURE 3.4: Modulating Excitation Intensity Doesn't Yield Information on Bond Lifetime. This chart plots the normalized photon counts as a function of force lifetime for different excitation intensities from 10^{-11} W to 10^{-3} W. The legend associates the colors each trace on the graph with different excitation intensities. The number next to the color corresponds to the common logarithm of the value of the excitation intensity ("-11" corresponds to 10^{-11} W). No consistent relationship between normalized photon count and force lifetime is observed, suggesting force lifetime information cannot be retrieved through modulating excitation intensity.

The next simulations probed the effect of probe excited-state lifetime on sensitivity. Plotting normalized emission by force lifetime curves for each luminophore lifetime appeared to indicate some responsiveness, but the plot is opaque. To clarify the data, I calculated the logarithm of the dynamic range, defined here as $\log(I_{max} - I_{min})$, where I_{max} and I_{min} are the maximum and minimum of the emission intensities (normalized as above). An ideal sensor would have a normalized I_{min} of 0 and I_{max} of 1, corresponding to a log-dynamic range of 1. **Figure 3.5** depicts a plot of log dynamic range versus luminophore lifetime.

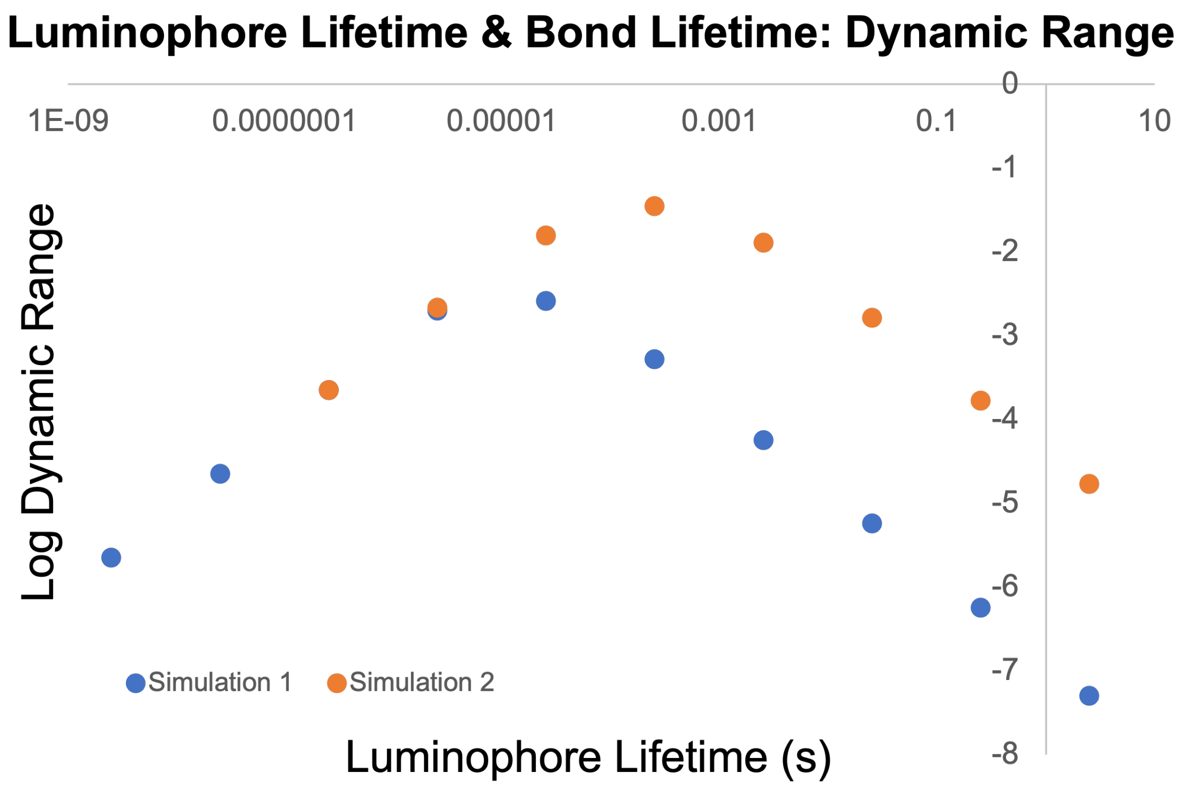

FIGURE 3.5: Dynamic Range increases, then decreases with increasing luminophore lifetime; the decrease results from numerical instability. Plotting the logarithm of the dynamic range (the logarithm of the difference between the probe's normalized emission intensities for the longest and shortest force lifetime), as a function of the luminophore lifetime suggests that increasing luminophore lifetime increases the dynamic range, up to an inversion point, after which it decreases (**blue** points). Modifying simulation parameters to delay the onset of numerical instability (**orange** points) delays the inversion, suggesting that the inversion is due to numerical instability. The overlap of blue and orange points at the 250 ns lifetime suggests the changes to the model's internal parameters made in the orange simulation set doesn't affect the model results when the system is numerically stable.

These results appear to indicate that the dynamic range first increases, then decreases with luminophore lifetime. This inflection point is counterintuitive and altering the simulation parameters to delay the onset of numerical instability (orange points) shifts the inflection point to the right, suggesting numerical stability drives this inversion.

Plotting the luminescence lifetime over the time taken to achieve steady state supports this theory (**Figure 3.5**). Assuming the probe force lifetime significantly exceeds the luminophore excited-state lifetime, the quotient of the time to numerical steady state (change rate <0.01%/sec) and luminophore lifetime should be relatively constant.

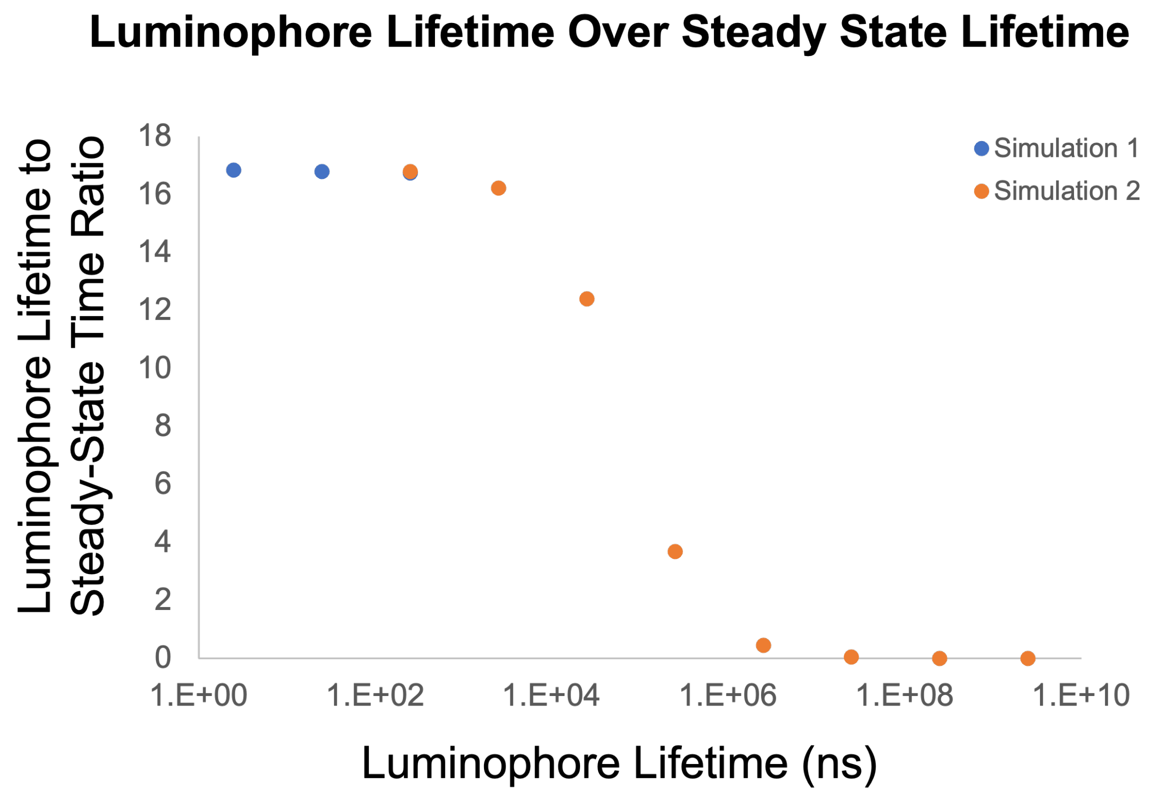

FIGURE 3.6: The ratio of luminophore and steady state lifetimes varies with luminophore lifetime, indicating numerical instability. Defining the ratio of the time taken to attain steady state (defined as a numerical deviation of <0.1% per second) and luminophore lifetime should be relatively constant. Plotting these values for the original simulation (blue) and the simulation modified for enhanced numerical stability (orange) illustrates a significant drop in the ratio, further supporting the conclusion that numerical issues are at play. The original simulation (blue) never attained numerical stability for luminophore lifetimes beyond 250 ns; thus, only three blue points are shown.

This curve is sigmoidal and drops precipitously near the luminophore lifetime of 25 μs, while the force lifetimes tested were 2-6 orders of magnitude greater than this value. Thus, the assumption of negligible force closure should be upheld with these conditions.

Even without this assumption, the data cannot be explained by changes in the force lifetime. While this steady-state-time to luminophore lifetime ratio does vary as force lifetime is increased, it changes by a maximum of 4% as the force lifetime increases over four orders of magnitude.[2] On the other hand, as the luminophore lifetime is increased from 2.5 μs to 25 ms, the value of this ratio decreases by ~93%.

The observed deviation's directionality can be intuitively understood. As the process lifetimes (luminescence, excitation) we consider increase, the corresponding kinetic rates decrease, and the absolute change-per-timestep in each parameter the Euler's method code calculates becomes miniscule – nearly indistinguishable from zero. The code likely interprets such small changes as evidence of the simulation having achieved a steady state, and prematurely halts the simulation, artificially decreasing the time-to-steady-state relative to the luminophore lifetime. This would artificially depress the ratio plotted above. Thus, numerical instability drives this inversion.

While numerical challenges severely curtail one's ability to extrapolate from this data, the trend itself appears promising and suggests that changing luminophore lifetime may illuminate the bond lifetime.

Signal and Signal to Background

I then examined the predicted photon counts. A heuristic analysis suggests a biphasic pattern: at first, when the lifetime of a probe in the ground state dramatically exceeds the luminophore lifetime, increases in luminophore lifetime will not significantly affect the net

---

[2] This maximum is reached in these simulations at 25 μs.

photon flux. As the luminophore lifetime increases beyond the lifetime, however, the rate limiting transition switches from excitation to emission, and the photon count will drop. The crossover point should occur as luminophore lifetime approaches the excitation lifetime, which, as previously calculated is ~71 μs.

This behavior seems to be recapitulated by the simulations. Plotting the logarithm of the average signal photon counts (across all force lifetimes) as a function of luminophore lifetime for both simulations appear to recapitulate this trend, as shown in **Figure 3.6.1**.[3] Unfortunately, the blue and orange simulations diverge, suggesting numerical instability drives some of this behavior. **Figure 3.6.2** plots the signal to background ratio by luminophore lifetime by both simulations. Since the emission rates of open and closed probes are identical, the signal-to-background ratio should be independent of luminophore lifetime. The observed, strongly sigmoidal profiles confirm that numerical instability contributes significantly to the decrease in log average signal.

Within the current model, the signal-to-background calculations are thus inconclusive.

Results Summary

1. The code appears (relatively) numerically stable for a fully open surface with Cy3B's excitation and emission parameters. However, these calculations need to be corroborated with microscope data.
2. Altering excitation intensity fails to resolve bond lifetime.
3. Altering luminophore lifetime appears promising, though instability precluded quantitative predictions. More stable simulations may help predict the photon counts and signal-to-background ratios.

---

[3] Due to numerical instability, the signal photon predictions hardly differed with force lifetime (**Figure 3.4**). Averaging them in this case is thus not misleading.

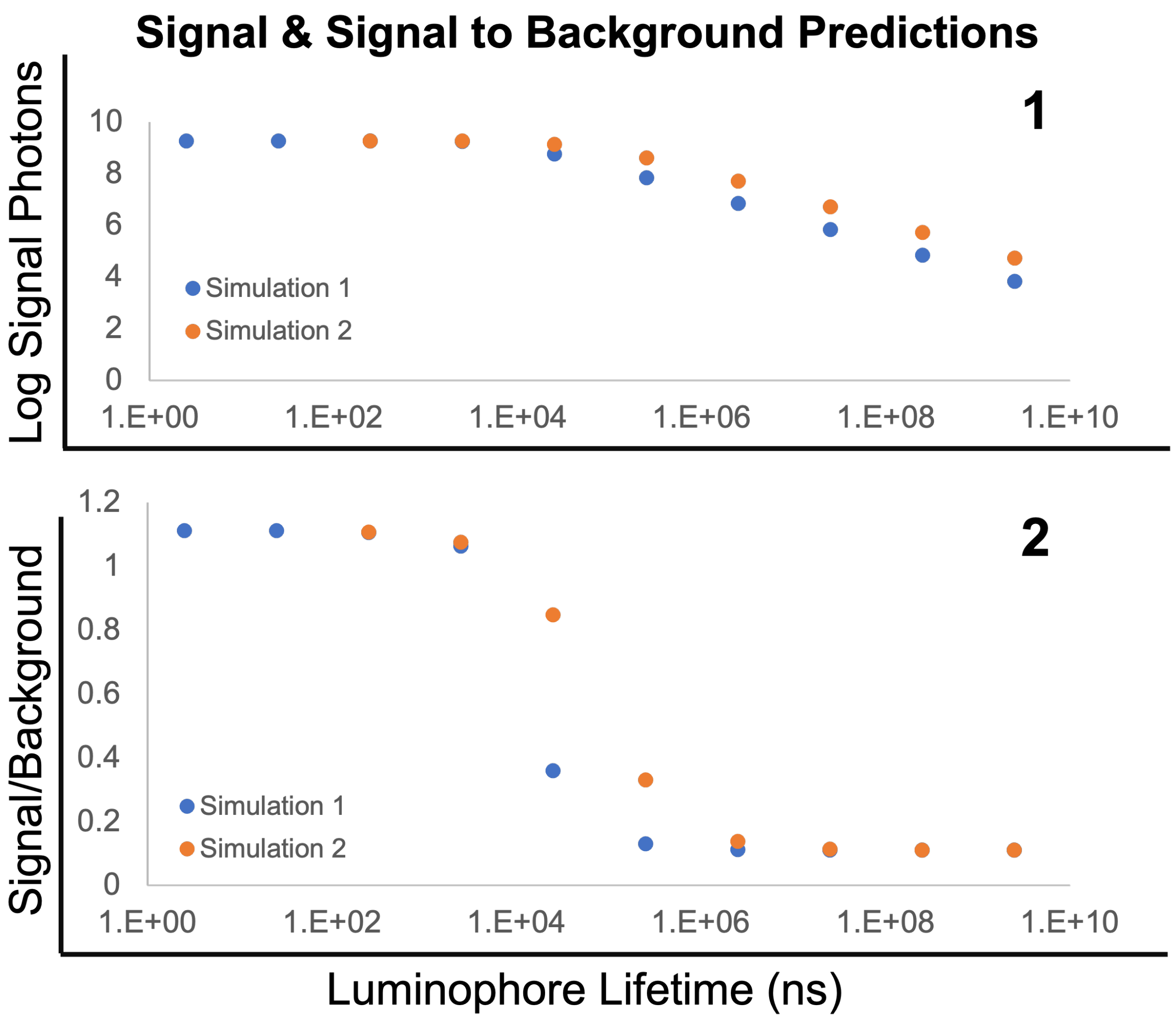

FIGURE 3.7: Signal and Signal to Background Predictions. (1) Plotting the logarithm of the predicted number of signal photons (photons arriving from open probes) as a function of luminophore lifetime indicates a decrease around 25 microseconds – which is close to the lifetime of the luminophore's ground state. However, the divergence between the two simulation runs suggests numerical instability may be present. Here, as before, the **blue** points indicate the original simulation while the **orange** ones indicate the less numerically unstable version. **(2)** To understand the magnitude of this instability we plot the signal to background ratio, defined as the ratio of photons from open probes (signal) and closed probes (background), against luminophore lifetime. Since the emission rate constants of open and closed probes are identical, this value should remain constant. The sigmoidal shape suggests numerical instabilities drive a large part of the observed behavior.

DISCUSSION

Simulation Limitations

The most apparent limitation of these simulations arises from numerical instability. These simulations stretch across a large parameter space: the excitation and emission rates span nine orders of magnitude while the force lifetime spans four orders of magnitude – this range intersected with the simply coded Euler's method implementation resulting in potential overflow and roundoff errors, leading to numerical instabilities. To save computer time, the code was designed to terminate if the system reached a numerical steady state. Unfortunately, the code's implementation rendered the system more susceptible to such numerical errors, especially as the process lifetimes increased. This susceptibility to instability also subtly restricted other parameters. Consider quenching efficiency: for these simulations the quenching efficiency of closed probes was held at 0.9. While this is less than the 0.95 for statically quenched Cy3B-BHQ probes [24], it kept k_{quench} and $k_{emission}$ values within a factor of 10, improving the model's stability. While this instability adds complicating factors, it doesn't preclude analysis.

Beyond instability, other subtle simplifications existed: it didn't consider instrument response function, camera gain, and noise, which become relevant at low photon fluxes, and would allow us to better understand whether a particular signal would be visible under a microscope. Furthermore, this model neglected the spatial distribution of opened probes, which may become important for low photon counts: a certain number of dim luminophores may be indistinguishable from background if distributed across the entire surface but may be reliably detected if concentrated in a small location. However, we deem these simplification minor since these simulations sought to test the basic *concept* of lifetime probes and not the feasibility of their implementation on a given camera and microscope system.

Potential Improvements

The simplest approach to navigating this numerical instability would employ existing packages that can solve differential equations (e.g. scipy, diffeqpy). Furthermore, it may be possible to mathematically transform the variables to minimize these range issues.

A more elegant solution arises by reframing the problem. The system of differential equations can be rewritten in matrix form as follows.

$$\frac{d}{dt}\begin{bmatrix} CG \\ OG \\ CE \\ OE \end{bmatrix} = K \bullet \begin{bmatrix} CG \\ OG \\ CE \\ OE \end{bmatrix}$$

Where:

$$K = \begin{bmatrix} -\left(k_{open} + k_{excitation}\right) & k_{close} & (k_{emission} + k_{quench}) & 0 \\ k_{open} & -(k_{close} + k_{excitation}) & 0 & k_{emission} \\ k_{excitation} & 0 & -(k_{open} + k_{quench} + k_{emission}) & k_{close} \\ 0 & k_{excitation} & k_{open} & -(k_{close} + k_{emission}) \end{bmatrix}$$

Or substituting *x* for our vector:

$$\frac{d}{dt}\vec{x} = K\,\vec{x}$$

Ultimately, we are concerned with the system's steady state behavior – that is, when the rates of change approach zero:

$$K\,\vec{x} = 0$$

This equation is a simple linear algebra problem: finding the null space of a matrix, which can be easily solved numerically with packages like NumPy. This reformulation would minimize the computational cost (the steady state conditions could be found within microseconds). While solving this linear algebra equation may still be numerically challenging due to the tremendous range of kinetic parameters, roundoff errors will not be magnified through iterative calculations.

Lowered Excitation Intensity

Numerical instability aside, the null result of the excitation intensity simulations is, retrospectively, expected: the model assumes that the mechanics and photophysics are separable. Since the rates of excitation depend solely on the laser excitation intensity and the spectroscopic properties of the dye, these rates are the same for dyes in open and closed probes. Thus, an open, ground state probe is no more likely to become excited than a closed, ground state probe.

But what if the mechanics and photophysics weren't separable? Consider static quenching, where a quencher that forms a specific complex with a luminophore that prevents its excitation [24]. If the effective absorbance of the luminophore/quencher complex were significantly less than the absorbance of the free luminophore, then opening the probe would dramatically increase the likelihood of the ground to excited-state transition – effectively turning the luminophore spectroscopically 'on'. The proportion of these *excitable* probes that become excited would then depend on the ratio of the rates of excitation and probe closing – and the resulting luminescence output would depend on the bond lifetime. This analysis would suggest that pairing suitably quenched probes with low excitation intensities may provide a useful approach to investigating bond lifetime, but further kinetic analysis is required.

Long Luminescence Lifetime

Though not definitive, the kinetic modeling suggests that long-lived luminophores may also reveal bond lifetimes. An ideal luminophore would have the following properties:

1. ~1 second emission lifetime.
2. Good quantum yield.
3. Suitably resistant to quenching by biologically relevant chemicals.
4. Efficiently quenched by the probe quencher.

Unfortunately, finding such luminophores is challenging. Many nonradiative process can quench luminophores, including vibrational transitions and triplet-state quenching by oxygen, and many organic room-temperature phosphorescent luminophores require crystallization, co-polymerization with another compound, or specific host-guest chemistries to suppress these transitions [50, 51]. Research continues apace to develop water-dispersible, oxygen-stable, long-lifetime luminophores for biological applications, and groups have reported biologically useful phosphorescent polymer encapsulated nanoparticles and nanocrystals [50, 51, 53, 54], but currently, their size (>100 nm) precludes their use for these DNA tension probes. Long-lifetime lanthanide-chelate-based luminescent dyes also exist – and while these are sufficiently small to be used in tension probes, their ~1 ms lifetimes are still three orders of magnitude too small for measuring second-scale bond lifetimes [52, 57]. Thus, such probes would rely on future advances in luminophore technologies.

The Photon Count Conundrum

Low photon counts present another challenge to both lowering excitation intensity and increasing luminophore lifetime. Consider a probe designed to measure an approximately 1 second bond lifetime. This probe must produce luminescent photons through a process with similar lifetime – this requirement constrains the maximum photon flux. Previously we calculated the ground state lifetime of a Cy3B fluorophore to be ~71 μs for a 1 mW excitation. Considering that the emission lifetime is ~2.5 ns, the timescale of this excitation-emission cycle process will approximate 71 μs. For any of these probes, however, the excitation-emission cycle timescale will be almost five orders of magnitude slower, approximating 1 second. Thus, for a given period, these bond-lifetime measuring probes will produce almost five orders of magnitude fewer photons than their standard fluorescent counterparts. While such detection may be possible – modern Electron Multiplying Charge Coupled Devices can register single-photon counts – it may complicate the acquisition of high-resolution images [58].

CONCLUSIONS

Developing probes with slow emission cycles to optically reveal bond lifetimes may theoretically be feasible, though it would require improvements in imaging and/or luminophore technologies to be implemented in practice.

Chapter 4: Tension Probes to Disentangle Force and Work in T-Cell Receptor Triggering

Special acknowledgements to J. Dale Combs for kindly mentoring me through this process, as well as to Anna Kellner, Joshua Brockman, and the mechanobiology subgroup for essential feedback and intellectual support.

INTRODUCTION

Whether regulating self-reactivity, triggering, coordinating, and executing tailored immune responses, or maintaining long-term memory of pathogens, T-cells underpin adaptive immunity. While many subtypes of T-cells exist – CD4+ T-cells, CD8+ T-cells, Tregs, and beyond – they develop similarly: emerging from the bone marrow, they migrate to the thymus where they are selected and mature, before passing to peripheral organs. When, in the course of an infection, a naïve T-cell encounters its antigen and co-stimulation and activates, dividing relentlessly and differentiating in a process known as clonal expansion to generate effector phenotypes to mediate immune clearance. Activated CD4+ *helper* T-cells act as conductors – releasing cytokines to orchestrate other immune cells. Activated CD8+ cytotoxic T-cells, by contrast, are assassins – scanning the body cell-by-cell to identify and kill targets. While most effector cells undergo apoptosis after successful pathogen clearance, some "memory cells" persist, ready to respond should the pathogen return [59].

For T-cells, accurate antigen recognition is vital, and the T-cell receptor (TCR) comprises the knife edge of T-cells' recognition system. The TCR faces a remarkable challenge of sensitivity and specificity: to detect and respond to traces of foreign antigens amidst a sea of very similar self-antigens. Experiments indicate T-cells can respond to single antigens amidst a sea of self-peptides and can distinguish between antigens differing by a single amino acid [60-63]. Furthermore, the same TCR can trigger subtly different responses to different antigens: in the thymus, weak TCR-antigen interactions are required for positive selection while strong responses trigger negative selection [48, 59, 64]. How is this attained?

Affinity experiments further convolute this puzzle. The 3D affinity of the TCRs for their antigen-peptide loaded Major Histocompatibility Complex (pMHC's) generally range from 1 to 100 μM and don't necessarily reflect a peptide's agonistic potential [2, 49, 60]. Indeed, some attempts to introduce higher affinity T-cell receptors into T-cells resulted in defective responses at low antigen concentrations [63]. 2D affinities, as measured between TCR's and peptide MHCs constrained in membranes, can correlate with agonistic potential, but the result isn't universal [2, 49], and one group discovered that certain agonistic peptides display faster *off-rates* than weak ligands [63]. Furthermore, 2D kinetic parameters measured in live T-cells better predict biological response than 2D kinetic measurements in membranes [49], and vary significantly from their 3D counterparts, though inhibiting the cytoskeleton abrogates this change [63]. Twinned questions emerge— what model and mechanism enable the TCR to achieve this sensitivity and specificity. If the model is an abstract recognition algorithm, the mechanism is its biomolecular implementation. Two main models have emerged to describe the abstract recognition "algorithm" of the TCR: Serial engagement and kinetic proofreading.

Serial engagement reconciles low affinity with extraordinary sensitivity by contending that multiple T-cell receptors serially engage a small number of peptide MHC's, producing an integrated biological signal that triggers activation. If the interaction is too weak, the bond lifetime is short, and the T-cell cannot reach the integrated signal threshold for activation.

If the interaction is very strong and the bond lifetime is long, the pMHC cannot bind enough TCRs quickly enough to activate the T-cell. If the lifetime is just right, a few pMHC's can serially engage many TCRs resulting in activation [63]. While serial engagement of a few pMHCs by multiple TCRs may occur, this model cannot fully explain TCR behavior [6, 65]. Studies searching for ideal, intermediate TCR-pMHC bond lifetimes – a key prediction of serial triggering – have yielded mixed results, and optical-trap based experiments that use force to lower the probability pMHC rebinding can still induce T-cell activation. [61, 65]. Furthermore, Chakraborty and Weiss argue that serial engagement trades sensitivity for specificity [61].

Kinetic proofreading provides an alternative. Conceptually, kinetic proofreading transforms a slight difference in lifetimes to a large difference in biological response by passing through a series of intermediate states, each of which can be reversed in one step to the starting state. Interactions with lifetimes long enough to "run the gauntlet" survive. As Weiss and colleagues note, this process must be far-from-equilibrium: the cell pays for the specificity and selectivity with energy. [61]

Decades of research have begun to resolve the silhouette of the T-cell-antigen recognition mechanism. At its simplest, the TCR itself consists of a heterodimer of alpha and beta chains, and is associated closely with another multimeric transmembrane protein, CD3. When TCR binds an antigen presented in an MHC molecule on the surface of another cell, a coreceptor – either CD4 or CD8 – is recruited, which also binds the peptide-MHC complex. This interaction brings LCK – a kinase associated with the coreceptor's cytoplasmic tail – in proximity both with Immunoreceptor Tyrosine Activating Motifs (ITAMs) in the cytoplasmic tails of CD3 and the TCR, as well as with Zap70, another kinase. Several phosphorylation reactions occur and Zap70 activates, relaying the signal to LAT, which recruits a signalosome that unleashes a cascade of biochemical processes that lead to the T-cell's response [2]. (**Figure 4.1**)

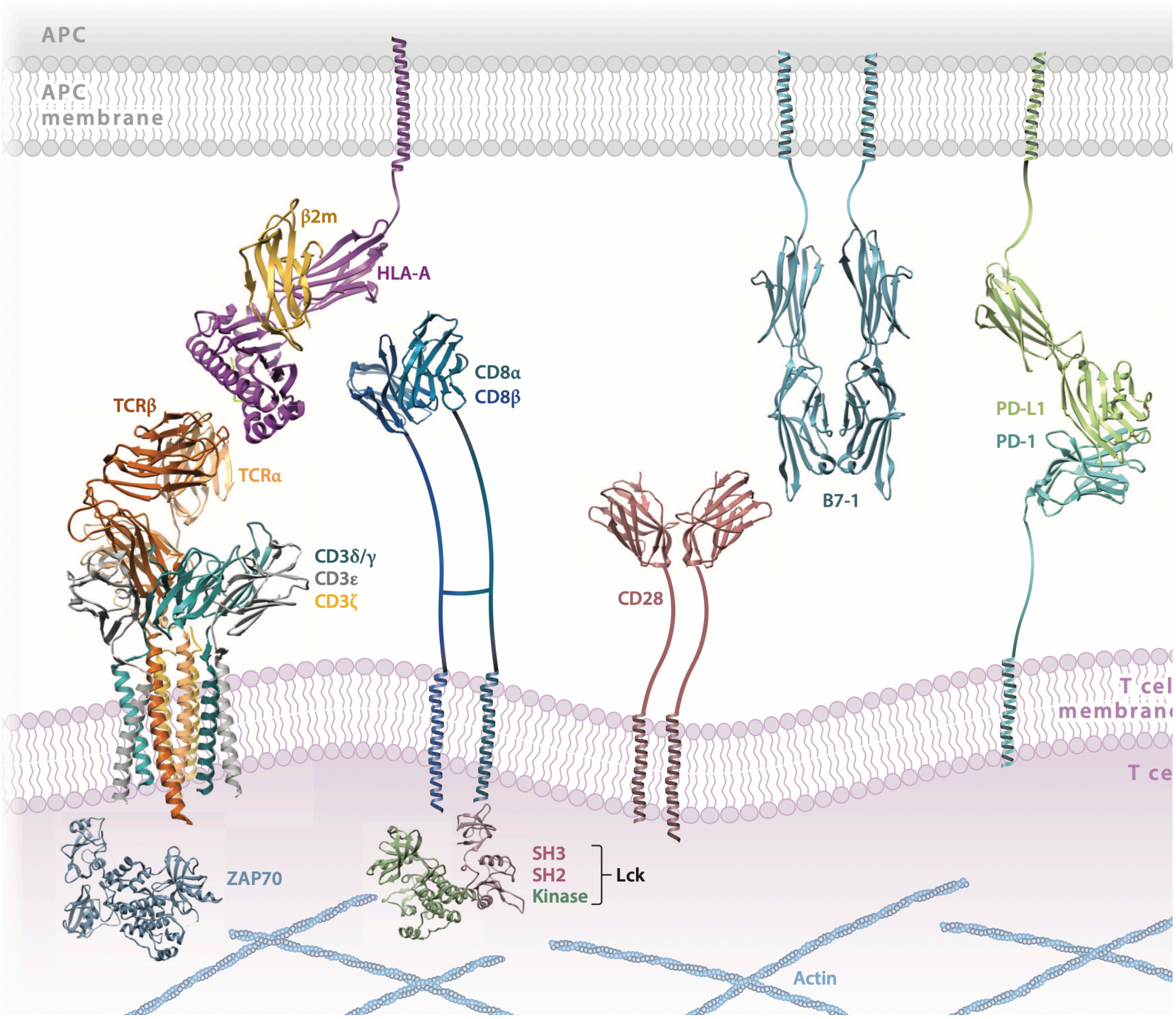

FIGURE 4.1: Schematic of T-Cell Receptor and Co-receptor MHC Interactions. TCR-CD3 complex interacts with Peptide-MHC (HLA) and the CD8 Co-receptor, bringing together LCK kinase with TCR and CD3 cytoplasmic ITAM tails (not shown) and ZAP70, triggering a series of phosphorylations and the T-cell signaling cascade. T-cell responses are also influenced by other receptor ligand interactions, such as CD28/B7-1 and PD-1/PD-L1 interactions. Figure reprinted from [2].

At higher resolution, however, consensus diverges, and a dizzying array of molecular mechanisms have been proposed to explain the TCR's sensitivity, specificity, and versatility. Two broad, potentially overlapping classes of mechanisms have emerged – those relying on changes in aggregation, clustering, or exclusion, and those invoking TCR conformational changes. Several lines of data suggest TCR clustering may be important for signaling. Artificial aggregation of T-cell receptors through cross-linking induces activation, and T-cells cluster their receptors upon activation [64]. Based on these results models have suggested that clustering and transactivation can serve to amplify the signal through the TCR. Other groups have suggested lipid rafts may be essential and have demonstrated that raft disruption through cholesterol sulfate interferes with T-cell activation [62]. A particularly popular model, kinetic segregation, contends that TCR-pMHC binding results in the physical exclusion of phosphatases from the cell-cell contact, shifting the dynamic equilibrium towards phosphorylation and receptor activation. Indeed, certain phosphatases like CD45 and CD148 are excluded from the immunological synapse, presumably because of their extracellular domain's steric bulk, and truncating this domain to inhibit this segregation interferes with T-cell activation [61, 64]. Other mechanisms hypothesize that conformational changes can transduce the TCR's signal and have proposed various allosteric mechanisms through which TCR ligation propagates through the TCR-CD3 complex and affects the accessibility of ITAM tails [66].

Multiple lines of evidence suggest mechanics – forces – may play a key role in TCR functioning. T-cells apply piconewton forces to pMHC's during activation [1, 20] and are activated far more effectively by surface-bound pMHC than by soluble monomeric pMHC[2]. Furthermore, the TCR is a mechanosensor: TCRs respond to substrate stiffness and force waveform [6], and force upon a small number of TCR's can result in T-cell activation [47, 67, 68]. Most intriguingly, several studies suggest key mechanical differences between TCR-activating and non-activating bonds. By studying anomalous, high-affinity non-agonist peptide MHC-TCR interactions, Sibener *et al* demonstrated that T-cell agonists formed catch bonds – bonds whose lifetime increases with force – with the TCR, while antagonists formed slip bonds – whose lifetimes decrease with force [49]. Another study from the Zhu group demonstrated that trimolecular "dynamic" catch bonds between the TCR, pMHC, and CD8 differentiated between negative and positive selection ligands in the thymus [48].

By adding a new dimension to this exploration of mechanism and model, mechanics can begin to bridge the two. Forces could conceivably induce conformational changes in the TCR-CD3 complex [66]. Furthermore, as Zhu and others note, kinetic segregation is an inherently mechanical process, influenced by the forces of membrane curvature and steric repulsion [6]. The enhanced lifetime of catch bonds could align with serial engagement's focus on the accumulated lifetime of interactions. Alternatively, as Brockman and Salaita note, mechanics could serve as a form of kinetic proofreading. Brockman proposes three generic mechanisms for this "mechanical proofreading." First, cells could select specifically for catch bonds by applying force and probing for bond lifetime. Second, cells could select for specific interactions by applying a given stress, defined as a force per unit area. This mechanism underpins the response of the B-cell receptor. Third, cells could probe for specific interactions through proteins that undergo large force-induced conformational changes. Only interactions capable of surviving the force required to induce the conformational change can induce signaling. This mechanism appears to be observed in integrins. These mechanisms can also work in conjunction to ensure maximal specificity [60].

As Ham and colleagues note, force isn’t the only dimension of mechanobiology, and reconciling apparent discrepancies between mechanobiological experiments demand that we examine other mechanical parameters [13]. Indeed, resolving mechanisms of mechanical proofreading requires looking beyond force. Here, we consider another such parameter: mechanical work. We develop probes with similar force thresholds but different work thresholds to open. By probing the difference between T-cells responses to these probes, we hope to better understand how energy and mechanical work intersect with these models of TCR signaling. This insight could ultimately improve our search for the mechanistic underpinnings of TCR signaling.

RESULTS

To distinguish the T-cell receptor’s sensitivity to force and work, we sought probes with similar predicted force thresholds ($F_{1/2}$) but that require significantly different amounts of work to open. Using the well-established 4.7 pN tension probe as a low-work control, we designed a probe with a similar opening force but a dramatically different extension. While the simplest design would just extend the length of the loop sequence – and we did consider one such design, we decided on a more intricate, double-hairpin construct that, if successful, would provide several advantages. The length of the construct enables us to span a large range of mechanical work, while the nested hairpins with independent dye readouts provide detail within that range. This design also offers more flexibility for follow on experiments: if the T-cell can only open the external hairpin, then one could lock the external hairpin open with a sequence complementary to that hairpin's stem-loop and probe whether the T-cell receptor can open the internal hairpin, thereby gaining additional information on the force/work/extension thresholds of the T-cell receptor; if the T-cell can open both, then time-correlated single molecule studies could potentially shed light into the loading rate and power output of the TCR. Finally, using the same hairpin for all these experiments dramatically simplifies controls, whether for surface density or construct length.

One can measure force and work of tension probes through various single-molecule force-spectroscopy approaches: optical/magnetic tweezers, and AFM. In practice, these experiments are non-trivial. Fortunately, Woodside and colleagues constructed a model, grounded in optical-tweezer measurements of a variety of hairpin sequences, to accurately predict force and work required to open hairpins. In brief, one can estimate the work of opening a hairpin as sum of the energy required to break the hybridization and the energy – as predicted by the worm-like-chain model – to extend the hairpin from its closed state [16].

Combining Woodside's model with the hairpin stabilities calculated by NUPACK at 25˚C [69], we calculated the work and force to unfold both the full hairpin and internal hairpins. A phase space of force by work depicts the location of several hairpins considered for this project and used in the lab. The points highlighted in red indicate the full and inner openings of the hairpin synthesized in this work, as well as the standard 4.7 pN hairpin sequence used for T-cell mechanobiological experiments. These force and work values should be interpreted with care: in both size and structure, the Ultramer hairpin differs drastically from the hairpins Woodside and colleagues probed, and absent single-molecule force-spectroscopy experiments, ascertaining the exact force and work requirements is difficult. Nevertheless, these data suggest the Ultramer hairpin design to be a good starting place. (**Figure 4.2**).

Using NUPACK, we next probed the entire construct for unexpected interactions between strands. While folding the Ultramer hairpin on its own yielded some off-target secondary structures, these occurred in regions with which full complements would exist and were thus deemed non-problematic. Examining the interactions between the dye-containing strands (DII, A21B, and Anchor) yielded no significant crosstalk. We additionally probed the locking strands for aberrant dimerization or secondary structure formation – while some was observed, the differences in energy between these assumed secondary structures and the full-complement is overwhelming. However, it should be noted this behavior may influence the kinetics of locking [20]. Furthermore, simulating the locking process by adding a 10x excess of lock strands, shunted the hairpin strongly into the open position, with 93% of the hairpin binding both outer and inner locking strands, and the remaining 6% binding the outer locking strand. (**Figure 4.3**)

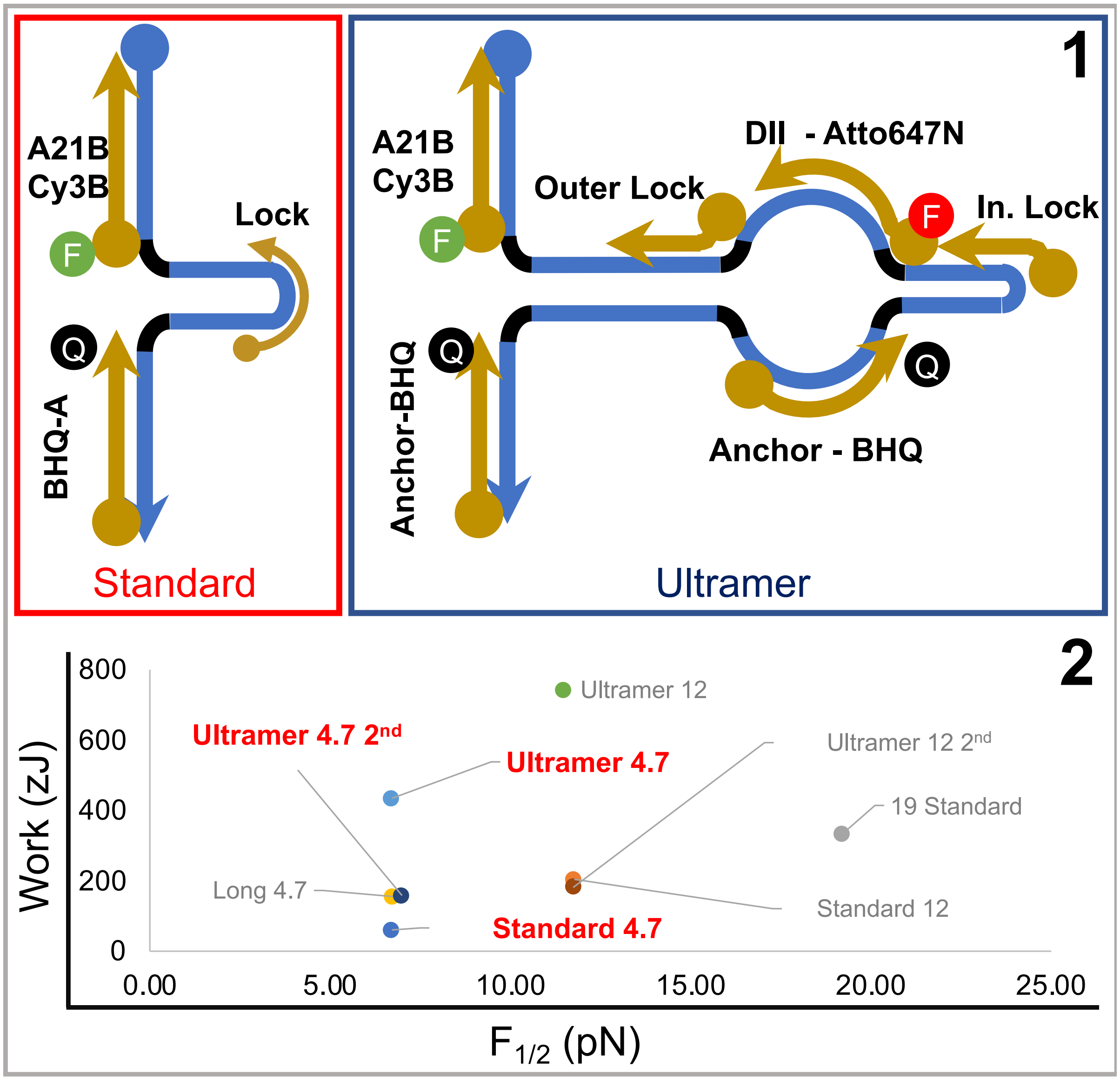

FIGURE 4.2: Hairpin Design and Phase Space. (1) Schematics of the Salaita Lab standard 4.7 pN hairpin and the Ultramer hairpin designed in this study. Strands are labelled with the names and dyes they are attached to. F indicates a fluorophore; Q indicates a quencher**. (2)** Phase space of force (zettajoules) by work (pN), calculated with formula developed by Woodside and colleagues. **Bolded, red** hairpins illustrate the constructs considered in this analysis. "Standard" hairpins have been tested experimentally in past [1]; "Ultramer" hairpins followed this double-design**.** The "long" hairpin corresponded to a single, 4.7 pN hairpin sequence with an extended loop, designed by Dr. Joshua Brockman and Anna Kellner, but not synthesized. Highlighted constructs display similar x-values, indicating similar opening forces, but dramatically different y-values, indicating different work requirements.

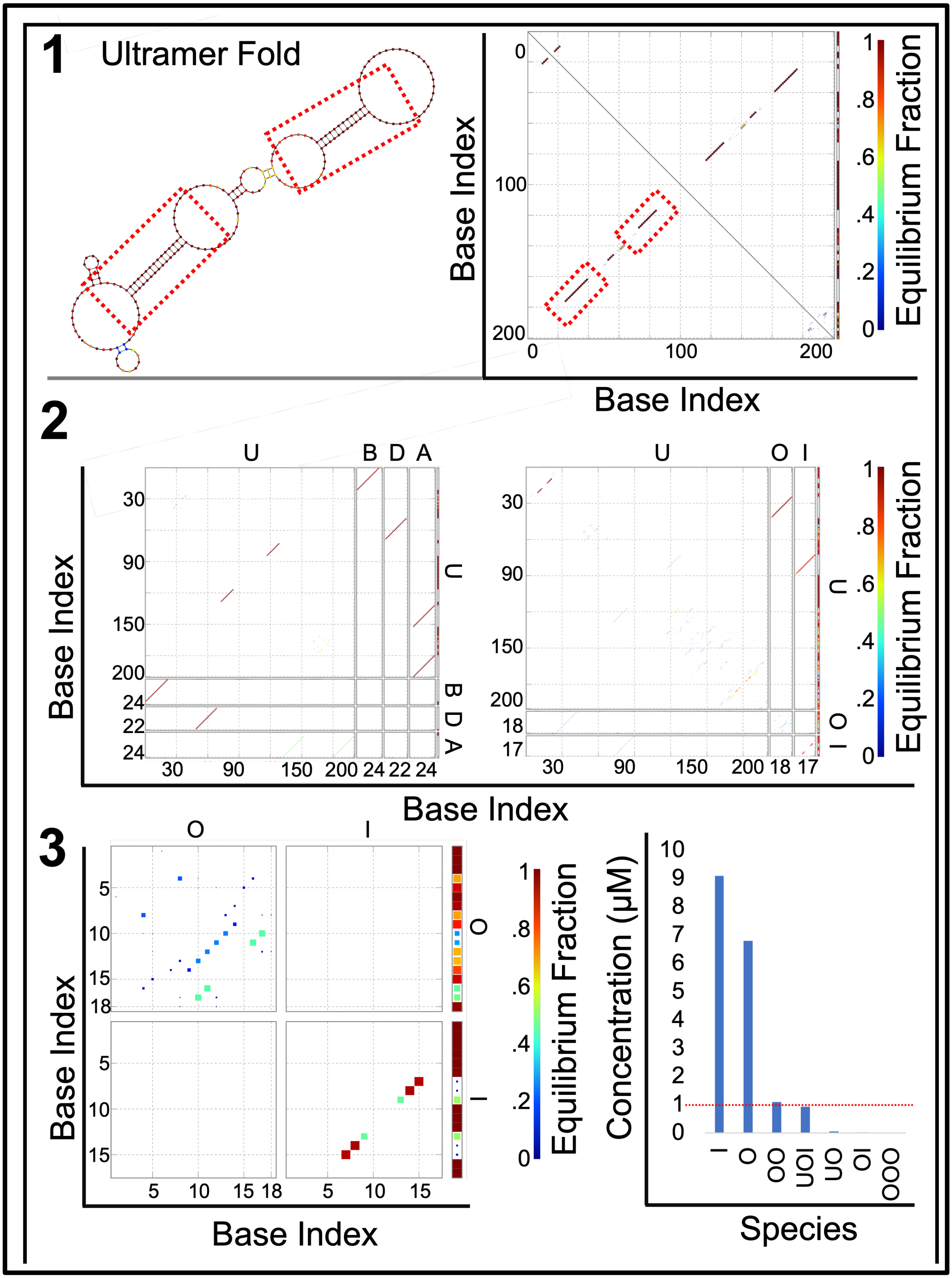

1
Ultramer Fold
Base Index
0
100
200
0
100
200
Base Index
1
.8
.6
.4
.2
0
Equilibrium Fraction
2
U
B
D
A
30
90
150
200
24
22
24
U
B
D
A
30
90
150
200 24 22 24
Base Index
U
O
I
30
90
150
200
18
17
U
O
I
30
90
150
200 18 17
1
.8
.6
.4
.2
0
Equilibrium Fraction
Base Index
3
O
I
5
10
15
18
5
10
15
O
I
5
10
15 18
5
10
15
Base Index
Base Index
1
.8
.6
.4
.2
0
Equilibrium Fraction
Concentration (µM)
10
9
8
7
6
5
4
3
2
1
0
I
O
OO
IOU
OU
IO
OOO
Species

FIGURE 4.3: Hairpin NUPACK verification. (1). Left: Computationally folding the Ultramer hairpin in NUPACK yields the following structure. The red, boxed regions indicate regions of self-complementarity that we expect for the hairpin. Other structures are seen, but their color is not a dark red, indicating a lower probability of forming. Furthermore, these regions are docking sites for other strands. Right: The graphs shown plot base pairing interactions within a grid where the nucleobase indexes of each strand form the grid's axes. Interactions between nucleobase x of one strand and y of another strand are plotted as a dot at (x, y), whose color corresponds to that interaction's equilibrium fraction. We see strong hybridization (evidenced by the red traces at 45 degrees) in two patches, circled in red; these correspond to the hairpin regions on the left. **(2)**. Left: Computationally folding 1μM Ultramer strand (U) with 1μM A21B (B), 1μM DII (D), and 2μM Anchor (A) yields the fully folded hairpin and displays no crosstalk. The dark red dots running at 45 degrees indicate strong hybridization, which we see observed in the expected locations for the interactions between the dye-labelled strands (B, D, A) and the hairpin (U). Interestingly, only one of the two hairpins is predicted to form under these conditions. Right: The inner (I) and outer (O) locking strands hybridize relatively strongly with the hairpin and disrupt most of the hairpin-hairpin interactions. Some self-binding of the hairpin still occurs, though not in bases we intended to hybridize. (3) Folding the lock strands upon themselves indicates some secondary structure and/or dimerization which may interfere with locking kinetics. (3) Locking strand strongly drive hairpin unfolding. Folding the 1 μM Ultramer (U), shown with the red dashed line, with 10x excess O and I locking strands yields 0.93 μM unlocked complex (UOI). Thus, locking secondary structure formation and dimerization (like the formation of the OO complex shouldn't preclude hairpin opening.

Ordering these fully modified strands is prohibitively expensive – we thus synthesized them from components. To the 3' amine modified DII strand we conjugated an Atto647N dye via NHS chemistry. HPLC purification yielded a product with absorbance at 260 nm (corresponding to DNA) and 647 nm, corresponding to the dye.

We similarly conjugated methyltetrazine to a 5' amine modified anchor strand, to which BHQ was attached. HPLC purification resulted in a peak with our putative product, which displayed absorbance at 260 nm (DNA) and 579 nm (BHQ). Though methyltetrazine has an absorption, it was masked by that of the BHQ. To confirm its conjugation, we thus folded the construct with the DII and anchor strands and attached it to a TCO conjugated surface. As compared to a negative control, conducted with fresh anchor strand yet unmodified with methyltetrazine, the putative product yielded a significantly higher fluorescence intensity ($p = 0.003$). Under the microscope, the putatively methyltetrazinelinked strand formed a uniform fluorescent layer, while the negative control was dark, save for a few patches of nonspecifically adsorbed strands. We interpreted these data to suggest the anchor strand was properly functionalized (**Figure 4.4**).

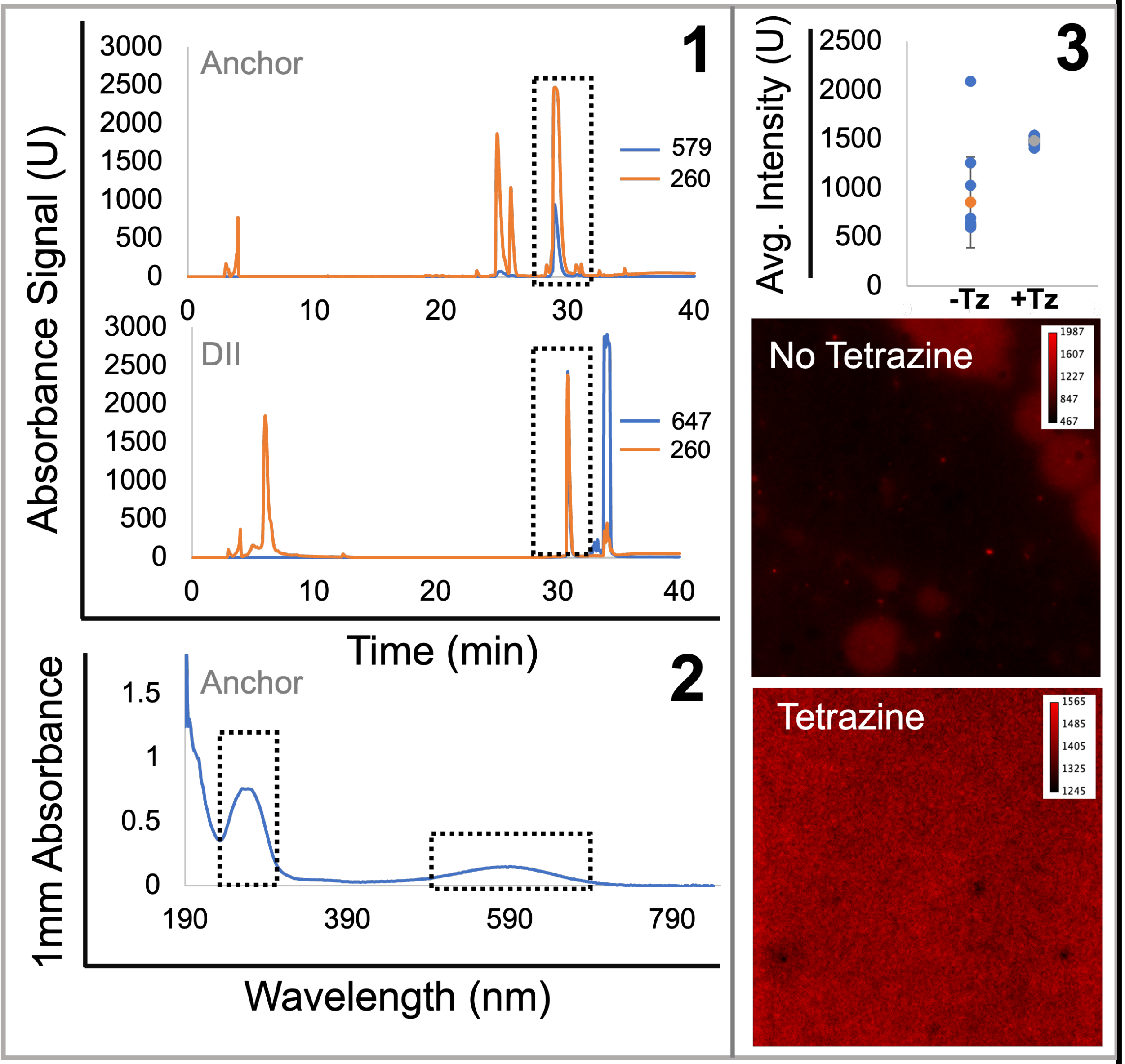

FIGURE 4.4: Strand Synthesis and conjugation. (1) Chromatograms of the NHS conjugations reactions with putative product peaks boxed. Runs were monitored for DNA by absorption at 260 nm (**orange**). Anchor strand (top) was also monitored for BHQ2 at 579 nm, while DII strand (bottom) was also monitored for Atto647N at 647 nm (**blue**). The double-peak before the band suggests some DNA separated from BHQ quencher. **(2)** Nanodrop spectra of Anchor strand confirms the BHQ quencher is still present. **(3)** TCO surfaces that were incubated with Ultramer hairpin, a fluorescent DII strand, and the putatively tetrazine-conjugated anchor strand were significantly brighter than surfaces incubated with hairpin, fluorescent DII strand, and anchor strand without tetrazine ($p = 0.003$) suggesting functionalization. The top graph illustrates the intensities, the bottom two illustrate representative images.

To simplify surface functionalization, we tested a silane-PEG-amine-based functionalization procedure. Anecdotally, biotin versions of these surfaces achieved very high functionalization density and precluded nonspecific binding, obviating blocking steps.

To test this chemistry, we functionalized the surface and quickly checked for amine presence by adding NHS-Cy5 dye to a portion of the surface. As compared to a negative control, the functionalized region displayed higher fluorescence, suggesting amine functionalization. After functionalizing with TCO, we attempted to attach our folded DNA hairpin to the surface. Images yielded background level intensity and repeating the experiment with new surfaces yielded a similar result, suggesting the DNA wasn’t attaching to the surface. Furthermore, we (and others in the lab) observed gel formation while dissolving the amine-peg silane in DMSO solvent to prepare to add to the slide, suggesting polymerization, perhaps due to reagent contamination or impurity. Furthermore, since T-cells do not produce ECM, the benefit of the PEG’s blocking effect is less significant. We thus deemed the silane coupling more trouble than it was worth (**Figure 4.5**).

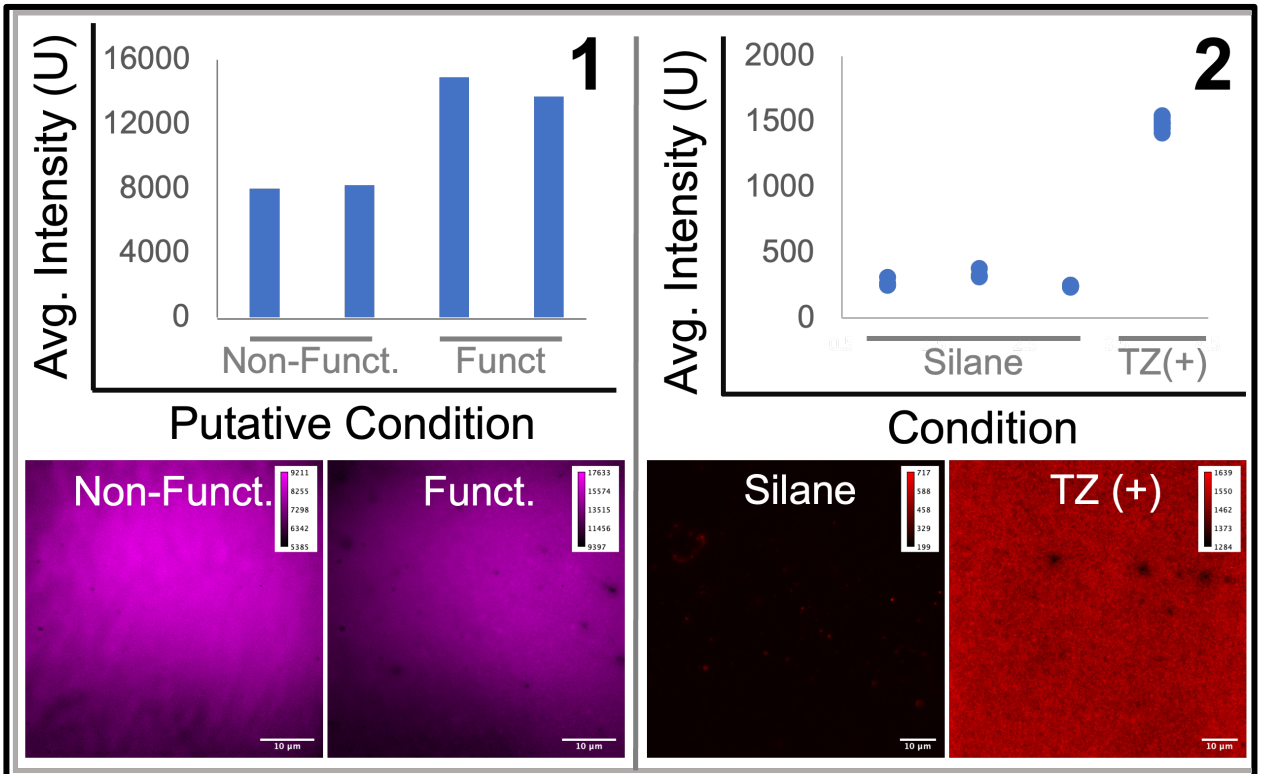

FIGURE 4.5: Silane Chemistry proved challenging with these surfaces. (1) Crudely testing for amination by adding Cy5-NHS ester to putatively functionalized and nonfunctionalized surfaces suggested that amination occurred, with the condition labelled "funct," showing higher background fluorescence than the condition labelled "non-funct" Representative images are depicted below. **(2)** Attempting to fold and add the hairpin to TCO surfaces made with this silane chemistry showed poor functionalization as compared with the surface used to confirm methyltetrazine conjugation (TZ). Representative images of both silane and the positive control are shown here.

Switching to APTES chemistry, we then asked whether these probes could observe cellular tension. We prepared Ultramer tension probe-functionalized surfaces (without BSA blocking) that presented a strongly agonistic anti-CD3 antibody. To facilitate rapid testing of different conditions, we used long glass slides (25 x 75 mm). Reflection Interference Contrast Microscopy (RICM) data demonstrated that mouse OT1 CD8+ T-cells adhered and spread on the surface. Epifluorescence imaging observed a clear tension signal in the Cy3B channel (corresponding to the outermost hairpin), suggesting that T-cells could open the hairpins' outer strands. Intriguingly, epifluorescence imaging of Atto647N channel seemed to illustrate a depletion directly underneath most cells, and visual analysis of the TIRF images suggest this may be the case. At least three features can conceivably induce signal depletion on rigid substrates: probe degradation that results in loss of fluorophore, increased quenching, perhaps due to enhanced proximity between fluorophore and quencher, and optical effects, whereby alterations in refractive index of the cell relative to the surrounding solution effectively attenuate the light entering the objective. Since the Cy3B and Atto647N fluorophores bind the same construct, and depletion is not observed in Cy3B, degradation appears unlikely. Furthermore, the proximity of Atto647N with its BHQ quencher implies that enhanced quenching is another unlikely explanation, as the predicted quenching efficiency should already be near unity. We thus suspected optical effects – changes in refractive index underneath the cell artificially depleting the amount of light entering the objective. However further investigation is warranted if this depletion is seen in future images. These data suggested that this tension probe design could measure cellular forces. Furthermore, the T-cells appeared to only open the outer probe – if reproducible, this finding could prove biologically insightful (**Figure 4.6.1, 4.6.2**).

On the same surface, we also tested the locking strands for their ability to lock open this hairpin construct. Through time-lapse imaging we quantified the increase in surface brightness after adding 10X molar locking strand. Successful unlocking would brighten the surface as it artificially forces tension probes into their open conformations. Unfortunately, the images and quantification illustrate no enhancement, suggesting the locking didn’t work (**Figure 4.6.3**).

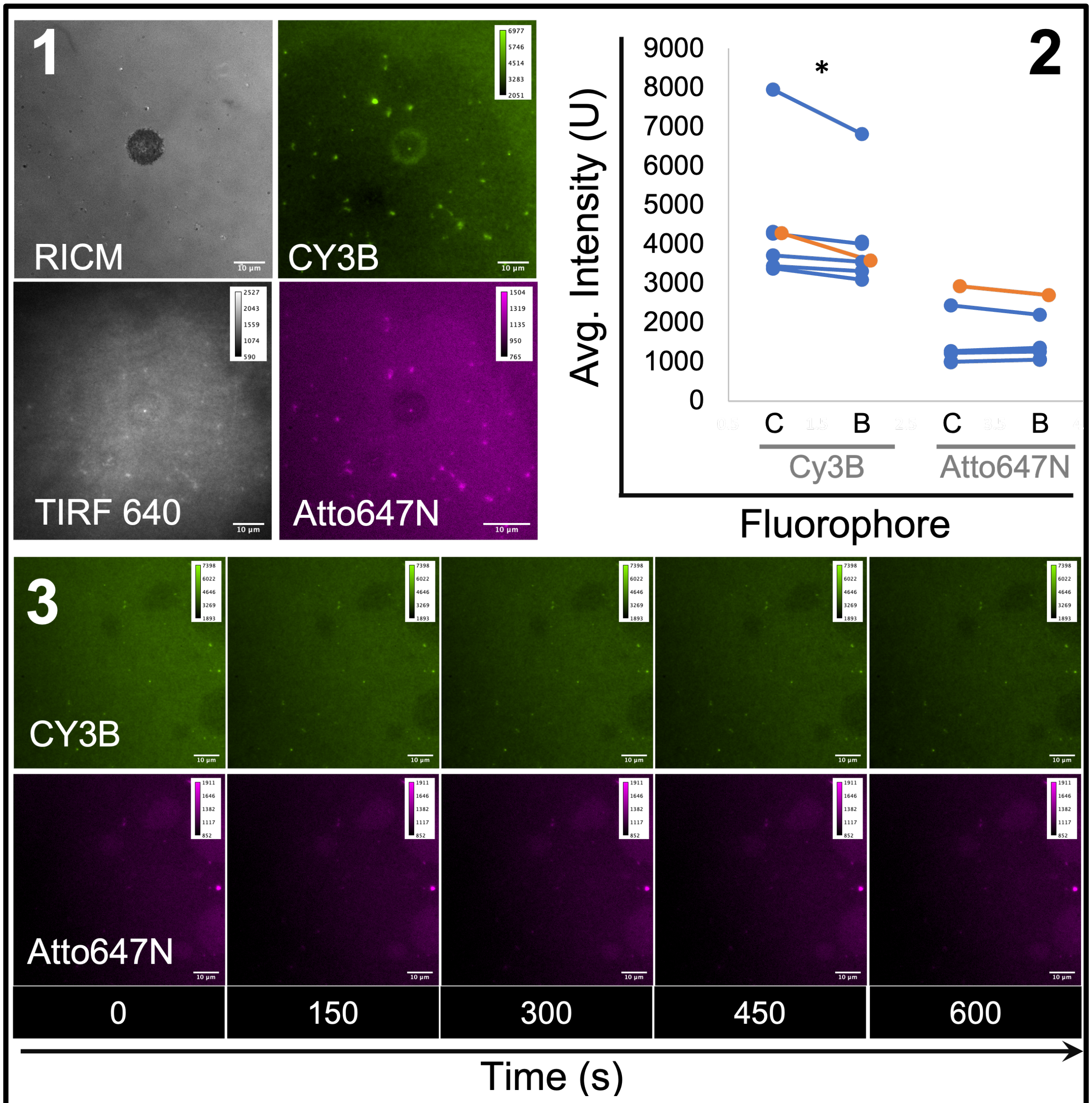

FIGURE 4.6: Double Hairpin Tension probes can detect tension in T-cells, but the locking strand fails to open the hairpin. (1) Reflection Interference Contrast Microscopy (RICM) shows cells spread on surface. Epifluorescence (epi) images of Cy3B (CY3B) indicate a clear, ringlike tension pattern. Epifluorescence in Atto647N (Atto647N) appears to show a depletion pattern, which may be recapitulated in 640 nm TIRF excitation. **(2)** Pairwise comparison of mean fluorescence intensity in cell (C) and background (B) regions suggests a significantly higher ($p = 0.0235$) CY3B tension signal under cells, with no increase in Atto647N. Orange, offset dots correspond to a cell for which only TIRF excitation data was taken. **(3)** Time series of surfaces upon addition of locking strand show no increase in intensity, suggesting locking didn't work.

These previous surfaces were blotchy, suggesting some nonspecific adhesion. After remaking surfaces in bulk, we began blocking with BSA to improve surface quality. We began by attempting to repeat the locking experiment, this time with BSA blocking. Three samples were prepared – one without any locking strands, a second folded with the outer locking strand, and a third folded with both locking strands. The images illustrate significant aggregation of DNA onto the surface, which we traced to minute salt crystals formed in the 1x PBS stock. This aggregation made the effects of lock strand addition challenging to decipher, though the numerical intensities suggest that, for the condition in which the outer lock strand was added, the Cy3 intensity appeared to increase. Unfortunately, this effect wasn't mirrored in the condition where both locking strands were added (**Figure 4.7.1**).

After filtering the 1X PBS buffer through a 0.22-micron filter, we attempted to remake the surfaces. After BSA blocking (1%, 5 minutes) we imaged to assess functionalization. The surfaces are extremely smooth, with no nonspecific binding: the sterile filtration adequately removed the salt, and the BSA block appeared to be effective. The surfaces are also devoid of any fluorescence signal, suggesting that the DNA wasn't effectively sticking to the surface.

Suspecting poor surface quality in my previous batch, I remade surfaces presenting the folded hairpins, decorated with anti-CD3 antibodies. To further promote functionalization, I added 40 picomoles hairpin instead of 20. Here, too, adding T-cells demonstrated no signal whatsoever (**Figure 4.7.2**).

Given that the construct had worked in the past, we suspected four mechanisms potentially driving these failures: first, degradation of the methyltetrazine anchor, which would prevent click conjugation to the surface; second, degradation of some hairpin component, which would likely preclude hairpin binding; third, systematically poor surface quality; fourth, interference from BSA. We decided to test all.

Electrospray ionization mass spectrometry (ESI-MS) analysis of the methyltetrazine-functionalized anchor strand yielded a charge-to-mass ratio of 772.7237 at z=11, from which we derived a mass of 8511.0487 Da. Using the mass from the manufacturer datasheets for our BHQ functionalized anchor strand (8093.4 Da), the methyltetrazine NHS ester (533.53 Da), and the NHS leaving group (115.09 Da), the calculated mass should be 8511.84 Da. The agreement to within 1 Da strongly suggests that methyltetrazine degradation is not to blame – loss of nitrogen gas (as occurs in the click reaction) would produce a shift of at least 28 Da on the mass spectrum, and a double-bond reduction would yield a 2 Da shift. Through a melting analysis we tested the hairpin's ability to fold – significant degradation of the hairpin's components would prevent the hairpin from folding, and thereby unfolding. Measuring the fluorescence intensity of the CY3B and Atto647N dyes as a function of temperature yielded clear melting curves, suggesting that the hairpin itself was intact (**Figure 4.7.3, 4.7.4**).

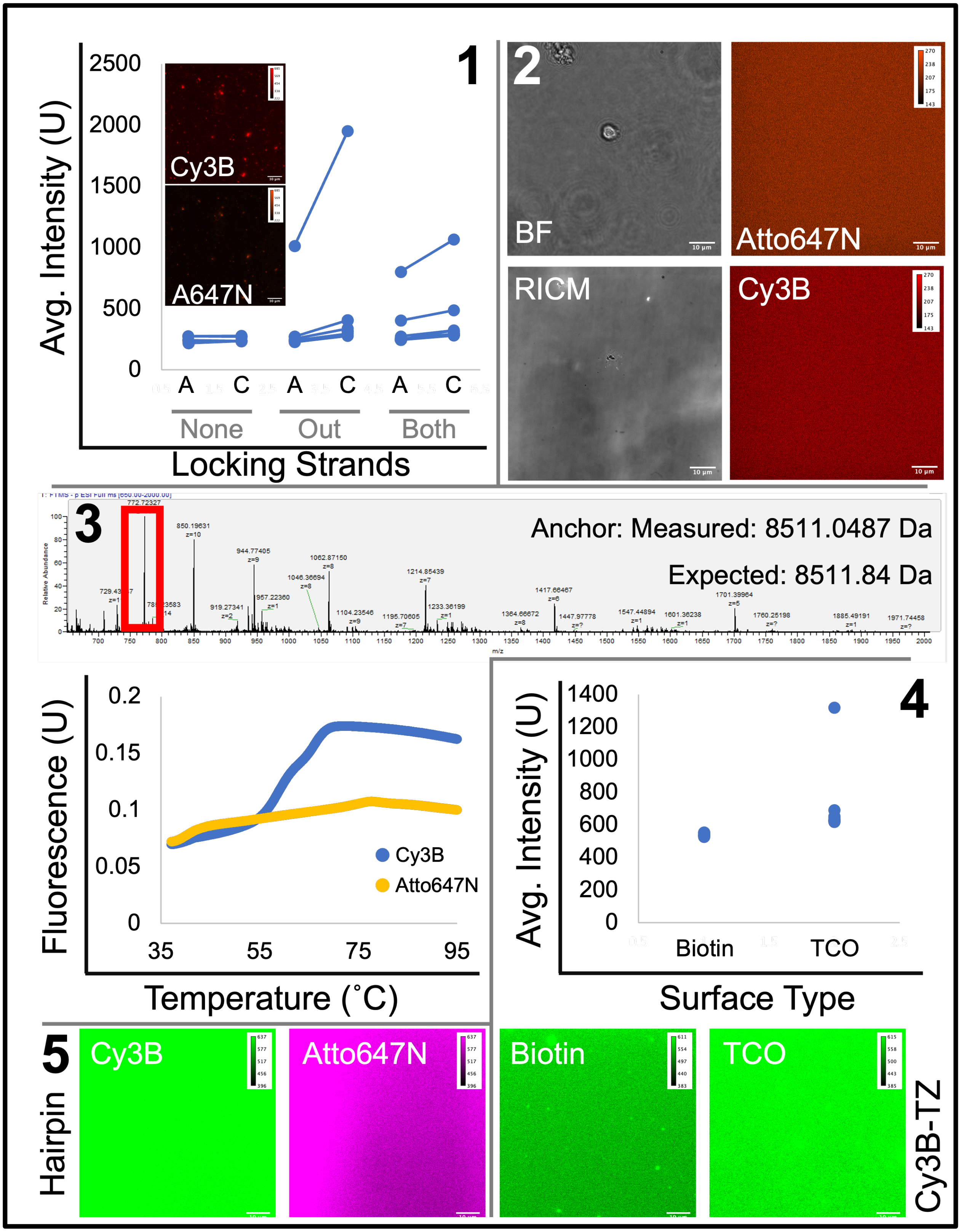1
Avg. Intensity (U)
2500
2000
1500
1000
500
0
Cy3B
A647N
A
C
A
C
A
C
None
Out
Both
Locking Strands
2
BF
Atto647N
RICM
Cy3B
10 µm
3
T: FTMS - p ESI Full ms [650.00-2000.00]
772.72327
850.19631 z=10
944.77405 z=9
1062.87150 z=8
1046.36694 z=8
1214.85439 z=7
1417.66467 z=6
1701.39964 z=5
729.43 z=1
919.27341 z=2
957.22360 z=1
1104.23546 z=9
1195.70605 z=7
1233.36199 z=1
1364.66672 z=8
1447.97778 z=?
1547.44894 z=1
1601.36238 z=1
1760.25198 z=?
1885.49191 z=1
1971.74458 z=?
Relative Abundance
m/z
Anchor: Measured: 8511.0487 Da
Expected: 8511.84 Da
Fluorescence (U)
0.2
0.15
0.1
0.05
0
35
55
75
95
Cy3B
Atto647N
Temperature (˚C)
4
Avg. Intensity (U)
1400
1200
1000
800
600
400
200
0
Biotin
TCO
Surface Type
5
Hairpin
Cy3B
Atto647N
Biotin
TCO
Cy3B-TZ

FIGURE 4.7: Ever Tried. Ever Failed. No Matter. (1) Reattempting the locking experiment yielded may have yielded an increase in intensity with only addition of the outer lock strand, but not with addition of both. A corresponds to Atto647N signal, C corresponds to Cy3B signal. Lines connect intensities from the same image position. Extensive aggregation, likely due to salt crystals, is seen in the images of these surfaces (inset). **(2)** Repeating the experiment with new surfaces and 40 picomoles of hairpin yields no functionalization and no T-cell tension. Brightfield (BF) image illustrates T-cell in image field. RICM displays strange filopodial morphology, suggesting T-cells are not finding ligand on the surface. Atto647N and Cy3B signals are at background, suggesting no functionalization whatsoever. **(3)** Top: ESI-MS of the tetrazine-containing anchor strand yielded the spectrum illustrated. Calculating the mass from the circled peak at m/z = 11 yields a value within 1 Dalton of its expected value, suggesting the strand isn't degraded. Bottom: Melt analysis illustrates clean melting in Cy3B and Atto647N channels, suggesting the hairpin strand is intact. **(4)** Top: On freshly synthesized long TCO surfaces I attached a Cy3B-Tetrazine to the surface as a positive control. When compared to a Cy3-Tetrazine-exposed biotin surface (which should display no binding), the TCO surface displays greater intensity. The P-value is ~0.06, but removing the top outlier drops that to <0.0001. These data suggest that tetrazine functionalization is weak. **(5)** Representative images of the TCO and biotin surfaces. Bottom left: Representative images of non-functionalization after attempting to attach a hairpin to these new TCO surfaces.

Suspecting low TCO functionalization density, we resynthesized TCO surfaces from long glass slides and attempted to reattach our hairpin. Since we hypothesized the TCO-NHS ester we dissolved and aliquoted in DMSO had hydrolyzed due to trace amounts of water in the DMSO, we repeated this experiment with 2.5 mg fresh TCO-NHS dissolved in 600 µL DMSO. To ensure DNA functionalization, we used 40 picomoles of the hairpin. To test for interference from BSA, we blocked with three different concentrations: 0.1%, 0.01% and 0% BSA. As a positive control we included a methyltetrazine-conjugated Cy3B dye,[4] which should attach to a TCO functionalized surface; as a negative control, we used a biotin functionalized slide. The results, shown below, strongly suggest a low TCO functionalization density. Even without BSA blocking, probe signal is, once again, absent, and while the positive control Cy3B-methyltetrazine dye incubated on the TCO surface demonstrates an increased signal relative to a CY3B-methyltetrazine incubated biotin surface, the increase is extraordinarily small. Since Cy3B is a small molecule, one would expect its functionalization density to be extremely high, and for a well-functionalized

---

[4] During these wash steps, we washed in 100% ethanol, as PBS would cause the extremely hydrophobic Cy3B-TCO/NHS ester to precipitate immediately onto the surface.

surface, this should produce an astronomical reading. Since we do not see this, we concluded that poor functionalization of the long slides with TCO was driving the observed problems (3.7.5).

In the Salaita Lab's experience, functionalizing the longer glass slides generally yields poorer results than functionalizing round coverslips. We thus switched to round coverslips. I prepared a batch of TCO functionalized coverslips and tested them with a fluorescently labelled, methyltetrazine containing strand. As a positive control, we used TCO functionalized circular coverslips prepared by another student for whom TCO surfaces were working well. As a negative control, we used TCO functionalized coverslips to which no fluorescently labelled DNA had been added. The results suggested robust functionalization with round coverslips in my hands. Using a coverslip from the same batch, we refolded the hairpin, conjugated it to the surface, and imaged. Once again, the image was at background (3.8.1).

Having established the integrity of the methyltetrazine-functionalized anchor strand, the functionalization of the TCO slides, and the correct folding of the construct, we hypothesized the concentration of a certain element of the hairpin construct was diminished. Due to partial degradation, we reasoned, a significant fraction of the hairpins was not forming. The fraction that did form correctly was enough to produce a signal during the solution-phase melting analysis but was too low to achieve the functionalization density required to image on a surface. Furthermore, since the methyltetrazine-labelled strand has a quencher, the entire surface is covered in a bed of quenchers, further diminishing any vanishing signal that may be present.

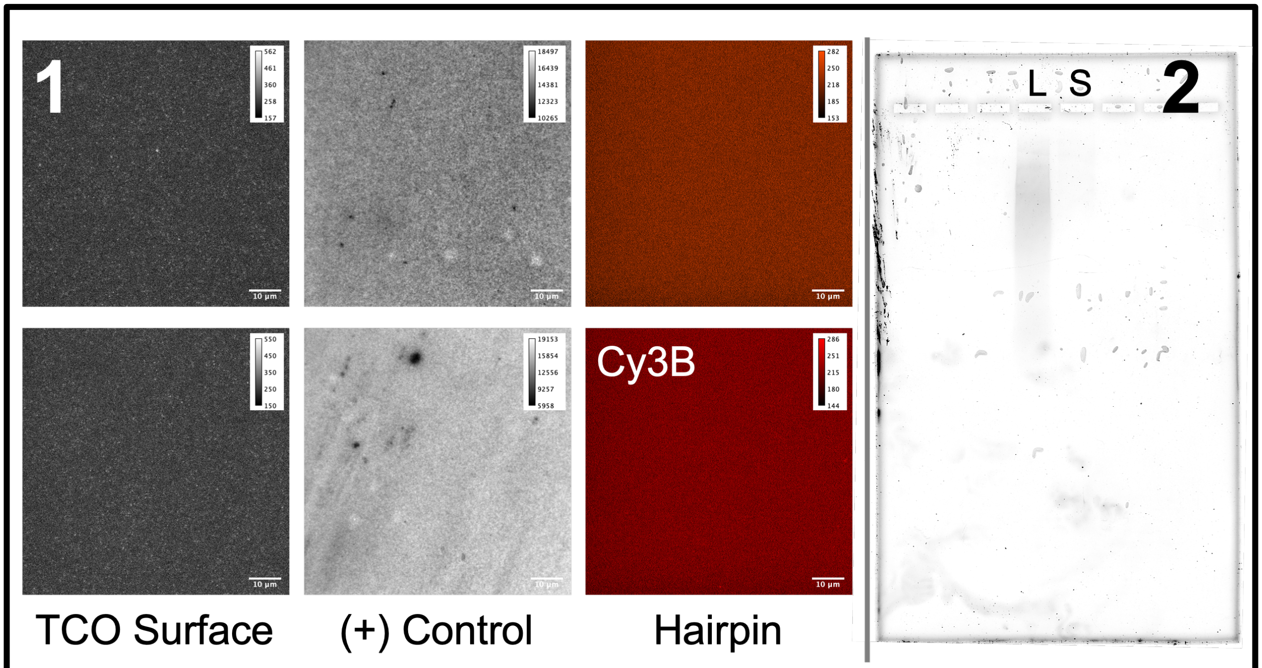

FIGURE 4.8: Try Again. Fail Again. Fail Better. (1). Testing functionalization with round slides. *Left*. Images from a TCO functionalized round slide to which no DNA was added shows no fluorescence (Mean Fluorescence ~200). *Middle.* A TCO functionalized slide with fluorescent, tetrazine-conjugated DNA is highly functionalized and fluorescent (mean fluorescence ~15000 U). *Right*. Adding Ultramer hairpin to these TCO surfaces yields no functionalization in Atto647N and Cy3B channels, evidenced by the low maximum intensity (~200). **(2)** Gel showing ladder (L) and sample (S). A faint sample band may be observable, but the ladder smearing makes it impossible to determine the sample band's molecular mass.

Two methods sprung forth to test the hairpin strand's integrity: mass spectrometry and electrophoresis. Due to the Ultramer hairpin's length (200 nt), the amount of sample required to run ESI-MS was unfeasible, so we chose the second path. The agarose gel we ran was inconclusive due to horrific ladder smearing (**Figure 4.8.2**). Furthermore, the DNA band wasn't clearly visible. At the time of writing, we plan to rerun this gel. Should this data suggest hairpin degradation, we would redesign and reorder the hairpin. Should the hairpin be intact, we would restart after repurifying each strand of the hairpin. The short-term goal would be to establish the essential controls: that the hairpin can be functionalized on the surface, that the strands can be locked open, and that T-cells can open these hairpins through force.

DISCUSSION

Hairpin Design

By applying Woodside's model, we assumed it extended to this double hairpin. Since the model was calibrated on a single hairpin, this may not be the case: the external hairpin could conceivably unfold at a significantly different force from the target value. [5] Nevertheless, we believe the assumption's general integrity: calculating the work to unfold the construct that would result from removing the internal hairpin and ligating the ends with a 3T spacer (to account for the ~2 nm distance) results in a calculated force of 6.98 pN, compared to 6.70 pN for the entire construct. Such a minute difference is unlikely to be relevant; as noted in chapter 1, single molecule force spectroscopy experiments on the standard 4.7 pN hairpin have yielded force values varying by over 2 pN, likely due to variation in buffer conditions.

In their analysis, Woodside and colleagues found that increasing loop length exponentially slows the unfolding process. As the loop length increased from 3 to 30 nt, the unfolding lifetime at $F_{1/2}$ increased over five orders of magnitude. Both loops of this hairpin construct exceed 30 nucleotides, suggesting that the kinetics of unfolding and refolding under force differ dramatically from that of the 4.7 pN hairpin. Such slow kinetics must be considered in any attempt to infer conclusions on the model or mechanism of TCR triggering.

---

[5] We are confident in the internal hairpin's unfolding since we recalculated that separately.

The current hairpin employs the same quencher strand sequence for the outer and inner fluorophore. Since this quencher strand is methyltetrazine functionalized, this design inevitably locks the hairpin to the surface in two places and makes the probe responsive – and resistive – to axial and lateral forces, further complicating biological interpretation. A future hairpin design would use a different quencher strand sequence for the inner hairpin.

Though inconclusive, the locking experiment suggested difficulties with locking kinetics. Comparing these locking strands to those developed by *Ma et al* [20] suggests that these strands are more likely to fold on themselves. A NUPACK analysis of the outer (18 nt) and inner (17 nt) strands, folded at 25C in 1M NaCl yields an energy of -1.55 and -2.26 kcal/mol respectively. Computationally folding Ma's 17 nt locking strand under the same conditions yields an energy of -1 kcal/mol. This extra energy required to unfold the locking strand may add a kinetic barrier to locking.

This double hairpin's length complicates lock design. Ma's 4.7 pN probe contained a 9 nt stem; the 17 nt locking strand, which hybridizes completely with one stem and the full loop, thus contains a large poly-adenosine sequence that is unlikely to induce secondary structure formation. This design uses 17 and 18 nt stem sequences containing all nucleobases. Since we designed the lock strands to hybridize completely with one half of the stem sequence, these longer lock sequences are more likely to form secondary structures. Future iterations should consider lock-sequence secondary structure while optimizing stem sequences. One may opt to hybridize the lock with part of the stem and part of the loop sequence, provided the locked state is still more thermodynamically stable than the unlocked one.

Finally, while simulations are powerful, they can only extend so far, and single molecule force spectroscopy studies would be essential to better understand the mechanical signature of these probes – their force extension curves and folding/unfolding rates – as T-cells experience them.

Biological Implications

The result that T-cells may be able to open the outer, but not the inner, hairpin raises intriguing biological questions on kinetic segregation and work gating.

Kinetic segregation argues the proximity of cell membranes in the immunological synapse sterically occludes large kinase ectodomains, and, as Blumenthal and colleagues note, experiments with fluorescent nanoparticles show that 16 nm quantum dots are excluded from the synapse [70]. Our data seemed to suggest that T-cells can open the outer hairpin but not the inner one. Assuming b-form DNA with 0.34 nm/nt, a single-strand contour length of 0.63 nm/nt, and a helix width of 2 nm, this distance sums to over 50 nm – far larger than the ~15 nm TCR/pMHC interaction and 16 nm quantum dots [70]. Thus, these data may contradict this component of kinetic segregation but are not definitive. However, since the hairpins are laterally immobilized, this extension could equally arise from lateral movement of TCR, and control experiments with hairpins on supported lipid bilayers – which cannot support lateral force – could separate these possibilities.

Since both outer and inner hairpins open at the same force threshold, these data suggest that the T-cell receptor pulling is not purely modulated by force – that something else must be present. Our primary hypothesis is that T-cells employ a work-gate, expending a certain energy to test an interaction in mechanical proofreading prior to triggering. However, conclusively proving this is complex: T-cells sense *and* respond to many aspects of the surface's mechanical properties, so establishing causality requires that one consider and control for many mechanical properties. These data could also be consistent with a distance gate, where the T-cell attempts to retract an engaged receptor through a certain distance before triggering, approximately aligning with the strain-sensing model of mechanical proofreading. These data could also be consistent with a time-gate, where the T-cells apply force for a certain amount of time on potentially activating interactions – if the interaction survives for that period, then the cell activates, in line with the lifetime alteration model of mechanical proofreading. Disentangling these possibilities would require careful controls that separate these possibilities from each other.

Consider differentiating work-gating from distance-gating hypotheses. One could link ligands to the surface with two different flexible polymeric linkers, one whose length equals the outer hairpin stem-loop sequence, the other whose length is between the length of the first and the total contour length of the double hairpin construct. Imagine as well that the work to extend these entropic springs was less than the work to open the outer hairpin of the construct used in this study. If the short linker activates but the long-linker doesn't, then we conclude that T-cells employ distance gating. If linkers induce similar activation, then we conclude that T-cells don't employ distance gating. Of course, this analysis predicates on an accurate biochemical measure of activation, for which we would need to gather data.

However, the T-cell could be sensing a dynamic combination of force and distance that depends on mechanical and chemical contexts. Indeed, given T-cells' extraordinary adaptability, this is likely the case. In this case, inferring the model of TCR triggering demands that we probe T-cells' responses to a huge number of mechanical properties and combine these data with more reductive, mechanistic studies of the TCR.

Finally, while powerful, this system has limitations. Crucially, these surfaces are inherently non-biological. In the body, TCR-pMHC interactions occur at curved, softer, cell-cell contacts within the context of other ligand receptor interactions; our surfaces, by contrast, are stiff, flat glass surfaces that present immobilized activating ligands. Many mechanochemical signals that likely inform T-cell antigen recognition cannot be included in this system. While these experiments are undoubtedly very useful to investigate the role of individual biological components, the experimenter must be cognizant of the implications of the system's limits. Further experiments could test these probes on steadily more biologically relevant systems – whether supported lipid bilayers or in actual cell-cell junctions.

CONCLUSIONS

This narrative suggests three relevant conclusions: first, that probes can be designed with similar $F_{1/2}$'s but drastically different amounts of work to unfold; second, that T-cells appear to be able to open the outer strands of these hairpins attached onto surfaces; third, Cumulatively, these data suggest that force isn't purely responsible for T-cell gating, though separating competing hypotheses – work, distance, time – demands further controls.

METHODS

Long Glass Coverslips: Piranha Functionalization

Long glass coverslips (75 mm by 25 mm) were cleaned by sonicating in 200 proof ethanol for 10 minutes, washed once in 200 proof ethanol, then baked dry at 95C. Surfaces were etched in piranha solution (66% v/v concentrated sulfuric acid, 33% v/v hydrogen peroxide (30% solution)) for 30 minutes, washed six times with water to remove all traces of acid.

Amine-PEG-Silane functionalization

Immediately after piranha functionalization, long slides were washed three times in ethanol and baked in an oven at 95C to remove all traces of water. 35 mg of amine-PEG-silane reagent were dissolved in 500 mL of dimethyl sulfoxide (DMSO) and added to freshly prepared piranha-functionalized long slides, which were subsequently baked at 95C for exactly 15 minutes. The resulting slides were sonicated three times in Nanopure water for three minutes each, followed by another three times in 200 proof ethanol for three minutes each, and then allowed to dry.

Surface Preparation: Long Slides, APTES

Immediately after piranha functionalization, the slides were base etched by sonicating at 4C in a 0.5M KOH solution for 30 minutes. After washing six times with water to remove all the base, and four times with ethanol to remove any traces of water, slides were placed in a 2% v/v solution of APTES (3-aminopropyltriethoxysilane) in 200 proof ethanol, covered in parafilm, and stirred for 1 hour. The slides were then washed three times in 200 proof ethanol, baked for 20 minutes at 95C, then washed another two times in 200 proof ethanol, baked for another 20 minutes at 95C, then stored.

Surface Preparation: Round Coverslips, APTES

Round coverslips were washed in Nanopure water, sonicated briefly, washed another three times in neat ethanol, sonicated briefly, then dried in an oven at 95C. The slides were piranha etched (66% v/v conc. Sulfuric Acid, 33% aqueous hydrogen peroxide (30%)) for 25 minutes, then washed six times in water and three times in ethanol. After adding fresh ethanol to the beaker and 1.5 ml of APTES was added. The beaker was sealed with parafilm to keep out moisture and allowed to sit for 40 minutes. The slides were washed with ethanol (3x) and dried.

TCO conjugation – Round Slides

TCO-NHS ester was dissolved at a concentration of 3-5 mg/ml in DMSO. 100µl was added to one round slide, and another slide was sandwiched on top, and allowed to incubate overnight.

Immediately prior to use, the sandwich is separated in ethanol, washed once to remove traces of DMSO, and dried.

TCO Conjugation – Long Glass Coverslips

400 µl 0.5 mg/ml TCO-NHS ester was added to an amine-functionalized long slide. Another slide was sandwiched on top. After an overnight incubation, the slides were separated in ethanol, washed once more in ethanol to remove DMSO, and dried. These long slides were mounted, either in an Ibidi chamber or onto a 96 well plate, prior to use.

Hairpin Folding

Unless otherwise specified, 20 pmol hairpin construct was prepared at a concentration of 1 µm in 1x PBS. 20 pmol of each component (hairpin, DII strand, A21B), are added to the solution, except for the anchor strand, of which 40 pmol are added. To fold, the hairpin is heated to 95C for 5 mins, then cooled to 25C.

Hairpin Surface Conjugation

For long slides, the surface was washed three times with 1 ml 1x PBS. Surfaces were blocked with BSA (0.1%, 30 minutes), washed another three times with 1 mL 1x PBS. On the final wash, PBS was removed through vacuum aspiration until the minimum amount of liquid to cover the slide remained. The folded hairpin mixture was then added to the solution and allowed to incubate for 30 minutes. If the reaction was to stay for an extended period, 2M sodium chloride solution was added to a final concentration of 1M NaCl (not including the sodium and chlorine already present in PBS).

Anti-CD3 Functionalization and T-cell Addition

Hairpin-functionalized surfaces were washed three times with 1 mL PBS. Streptavidin (2µg in ~90 µl total volume for Ibidi chamber, 5 µg for ~ 200 µl for 96 well plate) was added to the surfaces and allowed to incubate for 30 min. Surfaces were washed (3x with 1x PBS). Biotinylated Anti-CD3 antibody (40 µg/mL) was added to the surfaces, allowed to incubate for 45 minutes, then washed with PBS as above. The channels were filled with Hanks Buffered Saline Solution (HBSS), and T-cells (7-10K) were added. After incubating for 10 minutes, the cells were image.

Locking Strands

Lock strands were added at a 10x molar excess (e.g. 200 pmol lock strand for 20 pmol hairpin).

Methyltetrazine Conjugation

100 µg of methyltetrazine NHS ester was dissolved in 10 µL acetonitrile. 6 µL of 1 mM anchor strand, 2 µL 10x PBS, and 2 µL 1 M Sodium Bicarbonate were mixed and added to the dissolved methyltetrazine-NHS ester. The reaction was incubated at room temperature for 45 minutes. Final concentrations are below:

1. 5 mg/mL methyltetrazine-NHS ester
2. 300 µM Anchor strand.
3. 0.1M sodium bicarbonate.
4. 50% Acetonitrile
5. 50% 2x PBS

Net volume: 20 µL

A spin-column was prepared. 650 µL P2 gel in Nanopure water was added to a spin-column tube and spun at 14.7K RPM for 1 minute on a benchtop centrifuge to pack the column. After the residual water was removed from the bottom, the crude reaction mixture was added to the column and spun through at 14.7K RPM for 1 minute. The eluate was injected onto an Agilent AdvanceBio Oligonucleotide column and subject to a gradient elution. Flow rate: 0.5 ml/min. Solvent A: 0.1 M TEAA; Solvent B: Acetonitrile. Gradient Starts at 90% A, 10% B and increases at 0.5%/min B [21]. The product was purified via HPLC, with a retention time ~28 minutes.

Attempting this reaction without salt and bicarbonate led to lower yields.

Atto647N Conjugation

1. 5nmol DII strand
2. 1µL 10x PBS
3. 1 µL 1M Sodium bicarbonate
4. 1 µL Nanopure water
5. 1µL Atto647N-NHS ester dissolved in DMSO (excess).

This was incubated for an hour under sonication at room temperature, before being purified as above with methyltetrazine, first by a spin column and then by HPLC. The product retention time was approximately 31 minutes.

Hairpin Melting Analysis

20 pmol of the hairpin, at a concentration of 1 µM, was prepared as detailed in hairpin folding, diluted to 100 nm, and aliquoted into 10 wells of a 96 well plate used by the Roche LightCycler Instrument. The melt-curve program first held the sample temperature at 37˚C for 300 seconds, followed by a steady ramp of 0.04˚C/second until

a temperature of 95˚C was reached. The program was repeated twice to measure fluorescence in both Atto647N and Cy3B channels.

Electrophoretic Gel Separation

A 3.5% agarose gel was prepared by mixing 1.75 g of agarose with 50 mL Tris-Acetate-EDTA in a 250 mL flask, microwaving until the solution was clear and homogenous, then casting in a gel tray. 20 µL 100 nM of the Ultramer hairpin strand was mixed with loading dye and loaded into one well, while a ladder was loaded into another. The gel was run at 100 volts for 55 minutes at room temperature. The gel was stained by incubating in 100 mL of TAE to which 10 µL Diamond nucleic acid stain had been added.

Sequences

Name	Sequence	Notes
4.7 pN Ultramer Hairpin	`GTG AAA TAC CGC ACA GAT GCG TTT CCG GAC GCG TGT ACC TTT TTT TTC CGG AGG GCC TCA GTG TTA TGT TTT GTG CAG TGT GCG TTT TTT TTT TTT TTT TTT TTT TTT TTT TTT TT CGC ACA CTG CAC TTT AAG AGC GCC ACG TAG CCC AGC TTT TTT TTT GGT ACA CGC GTC CGG TTT AAG AGC GCC ACG TAG CCC AGC`	Long Hairpin Strand
DII Strand	`/5AmMC6/ ACA TAA CAC TGA GGC CCT CCG A`	Conjugated to Atto647N via NHS coupling
Anchor Strand	`/5AmMc6/ TTT GCT GGG CTA CGT GGC GCT CTT /3BHQ_2/`	Conjugated to Methyltetrazine via NHS coupling.

A21B	/5AmMC6/ - CGC ATC TGT GCG GTA TTT CAC TTT - /3Bio/	Conjugated to Cy3B via NHS coupling.
Outer Locking Strand	5′ AAA GGT ACA CGC GTC CGG 3′	
Inner Locking Strand	5′ AA AAA CGC ACA CTG CAC 3′	
4.7 pN Long Loop	GTG AAA TAC CGC ACA GAT GCG TTT GGC TTCG CGG GTT TTT TTT TTT TTT TTT TTT TTT TTT TTT TTT TTT CCC GCG AAGC CTT T AAG AGC GCC ACG TAG CCC AGC	Designed by Anna Kellner and Dr. Joshua Brockman. Not synthesized for this project.
Standard 4.7 pN Hairpin	GTG AAA TAC CGC ACA GAT GCG TTT GTA TAA ATG TTT TTT TCA TTT ATA CTTTAA GAG CGC CAC GTA GCC CAG C	[20]

Chapter 5: Conclusions

This work sought to explore the reciprocal relationships between tension probe structure, function, mechanical signature, and cellular responses.

In the first chapter, molecular dynamics simulations illuminate tension probe's structural sensitivity to sequence perturbations. Removing the 3-nucleotide spacers from the arms of the nicked three-way junction clearly interferes with proper folding, while the addition of a 5-nucleotide overhang appears less significant (**Figure 2.1**). In conjunction with Roxanne Glazier's photophysical data, these models suggest that these structural changes can tune probe photophysics. The structural model and accurately predicts that removing spacers brings quencher and dye closer, increasing quenching efficiency, but struggles to predict the effect of an overhang. However, such structural changes are unlikely to tunably influence the underlying mechanobiology of the system.

The second chapter mathematically models tension probes with slow photon emission rates to understand their ability to measure bond lifetime. These data suggest that slowing down photon emission rates through lowering excitation intensity wouldn't illuminate bond lifetime if fluorophore quenching is dynamic **(Figure 3.4)**, though static quenching remains unexplored. Furthermore, slowing photon emission through phosphorescence could theoretically allow bond lifetime measurement **(Figure 3.5)**, though advances in luminophore technology are necessary. Finally, any practical implementation would hinge on a solution to incredibly low photon counts.

The third chapter designs probes with similar opening forces but drastically different unfolding energies to disentangle what – force, work, or something more complex – do T-cells sense through their TCR. Our data suggest that we can design such probes that can be opened by T-cells, and that T-cells *may* test bonds with a work threshold versus a force threshold **(Figure 4.6)**. However, significantly more controls and replicates are required.

Scientific history is a dance between technology and theory: the former empowers us to gather new data; the latter to synthesize it into understanding and prediction. The relatively young field of mechanobiology is no different, and its growth depends on the simultaneous development of technologies to measure different aspects of cellular and molecular mechanics and the theoretical underpinnings to interpret these findings. This work aims to contribute to this integration.

REFERENCES

1. Liu, Y., et al., *DNA-based nanoparticle tension sensors reveal that T-cell receptors transmit defined pN forces to their antigens for enhanced fidelity.* Proc Natl Acad Sci U S A, 2016. **113**(20): p. 5610-5.
2. Liu, B., E.M. Kolawole, and B.D. Evavold, *Mechanobiology of T Cell Activation: To Catch a Bond.* Annu Rev Cell Dev Biol, 2021. **37**: p. 65-87.
3. Jansen, K.A., et al., *A guide to mechanobiology: Where biology and physics meet.* Biochim Biophys Acta, 2015. **1853**(11 Pt B): p. 3043-52.
4. Wang, J.H. and B.P. Thampatty, *An introductory review of cell mechanobiology.* Biomech Model Mechanobiol, 2006. **5**(1): p. 1-16.
5. Huse, M., *Mechanical forces in the immune system.* Nat Rev Immunol, 2017. **17**(11): p. 679-690.
6. Zhu, C., et al., *Mechanosensing through immunoreceptors.* Nat Immunol, 2019. **20**(10): p. 1269-1278.
7. Basu, R., et al., *Cytotoxic T Cells Use Mechanical Force to Potentiate Target Cell Killing.* Cell, 2016. **165**(1): p. 100-110.
8. Liao, J.C., et al., *Mechanochemistry of t7 DNA helicase.* J Mol Biol, 2005. **350**(3): p. 452-75.
9. Hansen, C.E., et al., *Platelet Mechanotransduction.* Annu Rev Biomed Eng, 2018. **20**: p. 253-275.
10. Li, Z., H. Lee, and C. Zhu, *Molecular mechanisms of mechanotransduction in integrin-mediated cell-matrix adhesion.* Exp Cell Res, 2016. **349**(1): p. 85-94.
11. Ma, V.P. and K. Salaita, *DNA Nanotechnology as an Emerging Tool to Study Mechanotransduction in Living Systems.* Small, 2019. **15**(26): p. e1900961.
12. Liu, Y., et al., *Molecular Tension Probes for Imaging Forces at the Cell Surface.* Acc Chem Res, 2017. **50**(12): p. 2915-2924.
13. Ham, T.R., K.L. Collins, and B.D. Hoffman, *Molecular Tension Sensors: Moving Beyond Force.* Curr Opin Biomed Eng, 2019. **12**: p. 83-94.
14. Grashoff, C., et al., *Measuring mechanical tension across vinculin reveals regulation of focal adhesion dynamics.* Nature, 2010. **466**(7303): p. 263-6.
15. Meng, F., T.M. Suchyna, and F. Sachs, *A fluorescence energy transfer-based mechanical stress sensor for specific proteins in situ.* FEBS J, 2008. **275**(12): p. 3072-87.
16. Woodside, M.T., et al., *Nanomechanical measurements of the sequence-dependent folding landscapes of single nucleic acid hairpins.* Proc Natl Acad Sci U S A, 2006. **103**(16): p. 6190-5.
17. Brockman, J.M., et al., *Mapping the 3D orientation of piconewton integrin traction forces.* Nat Methods, 2018. **15**(2): p. 115-118.
18. Ma, V.P., et al., *Ratiometric Tension Probes for Mapping Receptor Forces and Clustering at Intermembrane Junctions.* Nano Lett, 2016. **16**(7): p. 4552-9.
19. Glazier, R., et al., *DNA mechanotechnology reveals that integrin receptors apply pN forces in podosomes on fluid substrates.* Nat Commun, 2019. **10**(1): p. 4507.

20. Ma, R., et al., *DNA probes that store mechanical information reveal transient piconewton forces applied by T cells.* Proc Natl Acad Sci U S A, 2019. **116**(34): p. 16949-16954.
21. Brockman, J.M., et al., *Live-cell super-resolved PAINT imaging of piconewton cellular traction forces.* Nat Methods, 2020. **17**(10): p. 1018-1024.
22. Wang, X. and T. Ha, *Defining single molecular forces required to activate integrin and notch signaling.* Science, 2013. **340**(6135): p. 991-4.
23. Blanchard, A.T. and K. Salaita, *Emerging uses of DNA mechanical devices.* Science, 2019. **365**(6458): p. 1080-1081.
24. Glazier, R., et al., *Spectroscopic Analysis of a Library of DNA Tension Probes for Mapping Cellular Forces at Fluid Interfaces.* ACS Appl Mater Interfaces, 2021. **13**(2): p. 2145-2164.
25. Shaw, D.E., et al., *Anton 3: Twenty Microseconds of Molecular Dynamics Simulation Before Lunch.* 2021.
26. Hollingsworth, S.A. and R.O. Dror, *Molecular Dynamics Simulation for All.* Neuron, 2018. **99**(6): p. 1129-1143.
27. Lindorff-Larsen, K., et al., *Systematic validation of protein force fields against experimental data.* PLoS One, 2012. **7**(2): p. e32131.
28. Case, D.A., et al., *Amber 2021*, in *University of California San Francisco*. 2021.
29. Tan, D., et al., *RNA force field with accuracy comparable to state-of-the-art protein force fields.* Proc Natl Acad Sci U S A, 2018. **115**(7): p. E1346-E1355.
30. McCammon, J.A., B.R. Gelin, and M. Karplus, *Dynamics of folded proteins.* Nature, 1977. **267**(5612): p. 585-90.
31. Krieger, E. and G. Vriend, *New ways to boost molecular dynamics simulations.* J Comput Chem, 2015. **36**(13): p. 996-1007.
32. de Groot, B.L., et al., *Prediction of protein conformational freedom from distance constraints.* Proteins, 1997. **29**(2): p. 240-51.
33. Welch, J.B., D.R. Duckett, and D.M. Lilley, *Structures of bulged three-way DNA junctions.* Nucleic Acids Res, 1993. **21**(19): p. 4548-55.
34. Graen, T., M. Hoefling, and H. Grubmuller, *AMBER-DYES: Characterization of Charge Fluctuations and Force Field Parameterization of Fluorescent Dyes for Molecular Dynamics Simulations.* J Chem Theory Comput, 2014. **10**(12): p. 5505-12.
35. Best, R.B., et al., *Quantitative interpretation of FRET experiments via molecular simulation: force field and validation.* Biophys J, 2015. **108**(11): p. 2721-31.
36. Paquet, E. and H.L. Viktor, *Molecular dynamics, monte carlo simulations, and langevin dynamics: a computational review.* Biomed Res Int, 2015. **2015**: p. 183918.
37. Sengar, A., et al., *A Primer on the oxDNA Model of DNA: When to Use it, How to Simulate it and How to Interpret the Results.* Front Mol Biosci, 2021. **8**: p. 693710.
38. Pettersen, E.F., et al., *UCSF Chimera--a visualization system for exploratory research and analysis.* J Comput Chem, 2004. **25**(13): p. 1605-12.
39. Krieger, E., et al., *Fast empirical pKa prediction by Ewald summation.* J Mol Graph Model, 2006. **25**(4): p. 481-6.
40. Krieger, E., et al., *Making Optimal Use of Empirical Energy Functions: Force-Field Parameterization in Crystal Space.* Proteins: Structure, Function, and Bioinformatics, 2004. **57**: p. 678−683.

41. Essmann, U., L. Perera, and M.L. Berkowitz, *A smooth particle mesh Ewald method.* Journal of Chemical Physics, 1995. **103**: p. 8577.
42. Masliah, G., et al., *Identification of intrinsic dynamics in a DNA sequence preferentially cleaved by topoisomerase II enzyme.* J Mol Biol, 2008. **381**(3): p. 692-706.
43. Ulyanov, N.B., W.R. Bauer, and T.L. James, *High-resolution NMR structure of an AT-rich DNA sequence.* J Biomol NMR, 2002. **22**(3): p. 265-80.
44. Sokurenko, E.V., V. Vogel, and W.E. Thomas, *Catch-bond mechanism of force-enhanced adhesion: counterintuitive, elusive, but ... widespread?* Cell Host Microbe, 2008. **4**(4): p. 314-23.
45. Schoeler, C., et al., *Ultrastable cellulosome-adhesion complex tightens under load.* Nat Commun, 2014. **5**: p. 5635.
46. Hu, W., et al., *Mechanical activation of spike fosters SARS-CoV-2 viral infection.* Cell Res, 2021. **31**(10): p. 1047-1060.
47. Liu, B., et al., *Accumulation of dynamic catch bonds between TCR and agonist peptide-MHC triggers T cell signaling.* Cell, 2014. **157**(2): p. 357-368.
48. Hong, J., et al., *A TCR mechanotransduction signaling loop induces negative selection in the thymus.* Nat Immunol, 2018. **19**(12): p. 1379-1390.
49. Sibener, L.V., et al., *Isolation of a Structural Mechanism for Uncoupling T Cell Receptor Signaling from Peptide-MHC Binding.* Cell, 2018. **174**(3): p. 672-687 e27.
50. Tan, H., et al., *Crucial Breakthrough of Functional Persistent Luminescence Materials for Biomedical and Information Technological Applications.* Front Chem, 2019. **7**: p. 387.
51. Kenry, C. Chen, and B. Liu, *Enhancing the performance of pure organic room-temperature phosphorescent luminophores.* Nat Commun, 2019. **10**(1): p. 2111.
52. Cho, U. and J.K. Chen, *Lanthanide-Based Optical Probes of Biological Systems.* Cell Chem Biol, 2020. **27**(8): p. 921-936.
53. Siraj, N., et al., *Fluorescence, Phosphorescence, and Chemiluminescence.* Analytical Chemistry, 2016. **88**(1): p. 170-202.
54. Abdukayum, A., et al., *Functional near infrared-emitting Cr3+/Pr3+ co-doped zinc gallogermanate persistent luminescent nanoparticles with superlong afterglow for in vivo targeted bioimaging.* J Am Chem Soc, 2013. **135**(38): p. 14125-33.
55. Tokmakoff, A., *Time Dependent Quantum Mechanics and Spectroscopy*. 2021: Chem LibreTexts.
56. Cooper, M., et al., *Cy3B: improving the performance of cyanine dyes.* J Fluoresc, 2004. **14**(2): p. 145-50.
57. Cho, U., et al., *Ultrasensitive optical imaging with lanthanide lumiphores.* Nat Chem Biol, 2018. **14**(1): p. 15-21.
58. Coates, C. and A. Mullan. *What is an Electron Multiplying CCD (EMCCD) Camera?* 2021; Available from: https://andor.oxinst.com/learning/view/article/electron-multiplying-ccd-cameras.
59. Kumar, B.V., T.J. Connors, and D.L. Farber, *Human T Cell Development, Localization, and Function throughout Life.* Immunity, 2018. **48**(2): p. 202-213.
60. Brockman, J.M. and K. Salaita, *Mechanical Proofreading: A General Mechanism to Enhance the Fidelity of Information Transfer Between Cells.* Front Phys, 2019. **7**.

61. Chakraborty, A.K. and A. Weiss, *Insights into the initiation of TCR signaling.* Nat Immunol, 2014. **15**(9): p. 798-807.
62. Harrison, D.L., Y. Fang, and J. Huang, *T-Cell Mechanobiology: Force Sensation, Potentiation, and Translation.* Front Phys, 2019. **7**.
63. Valitutti, S., *The Serial Engagement Model 17 Years After: From TCR Triggering to Immunotherapy.* Front Immunol, 2012. **3**: p. 272.
64. van der Merwe, P.A. and O. Dushek, *Mechanisms for T cell receptor triggering.* Nat Rev Immunol, 2011. **11**(1): p. 47-55.
65. Feng, Y., E.L. Reinherz, and M.J. Lang, *alphabeta T Cell Receptor Mechanosensing Forces out Serial Engagement.* Trends Immunol, 2018. **39**(8): p. 596-609.
66. Schamel, W.W., B. Alarcon, and S. Minguet, *The TCR is an allosterically regulated macromolecular machinery changing its conformation while working.* Immunol Rev, 2019. **291**(1): p. 8-25.
67. Liu, Z., et al., *Nanoscale optomechanical actuators for controlling mechanotransduction in living cells.* Nat Methods, 2016. **13**(2): p. 143-6.
68. Hu, K.H. and M.J. Butte, *T cell activation requires force generation.* J Cell Biol, 2016. **213**(5): p. 535-42.
69. Zadeh, J.N., et al., *NUPACK: Analysis and design of nucleic acid systems.* J Comput Chem, 2011. **32**(1): p. 170-3.
70. Blumenthal, D. and J.K. Burkhardt, *Multiple actin networks coordinate mechanotransduction at the immunological synapse.* J Cell Biol, 2020. **219**(2).